When there is a discrepancy between the information in this technical report and information in JDox, assume JDox is correct.

STScI | SPACE TELESCOPE SCIENCE INSTITUTE

JWST TECHNICAL REPORT

Title: NIRISS On-Orbit Throughput Calibration	Doc #: JWST-STScI-008268, SM-12 Date: 27 September 2022 Rev: -
Authors: Kevin Volk Phone: 410-338-4409	Release Date: 22 November 2022

1 Abstract

The on-orbit photometric observations for NIRISS were used to derive corrections to the NIRISS throughput values used by the JWST Exposure Time Calculator. This report documents the process for calculating the various component throughput revisions. The derivation was a multi-step process, complicated by the inability to observationally isolate some of the components within NIRISS. As we only have constraints on the combined throughput in each mode and as there are redundancies between various of the modes the results have an element of ad-hoc decision making in terms of how to divide a given response function between the various internal components such as the internal optics and the detector quantum efficiency.

2 Introduction

The NIRISS instrument was not photometrically calibrated in the ground testing. The ISIM cryo-vacuum tests at Goddard Space Flight Center did not provide a calibrated external illumination source for testing the instruments. The first photometric measurements were obtained in JWST commissioning for the different NIRISS observation modes: imaging, wide-field slitless spectroscopy (WFSS), and single-object slitless spectroscopy (SOSS), and aperture masking interferometry (AMI). These measurements provide our first look at the NIRISS throughput values and overall photometric response.

Prior to launch the count rates for the different NIRISS modes were predicted by the JWST Exposure Time Calculator (ETC) using as input a set of assumed NIRISS and telescope properties: throughput functions for the optical telescope equipment (OTE), throughput functions for the internal components of NIRISS, and assumptions about the NIRISS detector response. These values were provided to the ETC in the form of a series of FITS table files giving response functions for different individual components, which are then used in the ETC to calculate the signal in electrons/second at the NIRISS detector for any of the configurations used for science. Additional inputs are needed for the ETC calculations, particularly point spread function calculations that are done using the "WebbPSF" package (Perrin et al., 2014).

The throughput and detector response functions for NIRISS were provided by the NIRISS STScI group in 2017, based upon a variety of ground testing results for NIRISS. The NIRISS component throughput measurements were a combination of vendor measurements for

the NIRISS filters and a set of measurements of the grism response done at the Université de Montréal by Loïc Albert and Mathilde Beaulieu prior to the final assembly of NIRISS.

In the case of the detector response the situation was more complicated than for the other components. A small number of quantum efficiency measurements were made of the detector by the manufacturer, Teledyne Imaging Systems, but attempts to fit the expected response function to these sparse points were not very successful. A decision was taken to apply the mean detector quantum efficiency and photon yield functions from a set of NIRSpec candidate detectors produced in the same "batch" as the NIRISS detector and measured in detail at the Goddard Space Flight Center, since we were not able to get such measurements for the NIRISS detector F17316 after it was delivered by Teledyne. This meant that the NIRISS detector response was not well known prior to JWST launch.

Finally, the telescope throughput estimate was provided by the JWST telescopes group and used by NIRISS and the other instruments. That part of the overall throughput is a fixed constraint that is used for interpretation of the NIRISS measurements.

Table 1 below lists the ETC input files used for calculations of the NIRISS photometric response. This includes the NIRISS filter and grism response functions and the grism dispersion values (number of μm/pixel, needed to calculate the signal per pixel in the dispersed spectrum). For the grisms spectral orders –1 and +3 are not used in the ETC calculations, but are still provided. The grism zero order response is not given for any of the grisms. In the SOSS mode the order 0 image is not on the detector for the science target, although order 0 images for other stars in the field may fall onto the detector. In WFSS mode the order 0 images are commonly seen but not dealt with in the ETC since they do not provide any spectral information.

Table 1: NIRISS input files for the ETC related to the photometric response

File Name	Description
jwst_niriss_f090w_trans.fits	F090W filter response
jwst_niriss_f115w_trans.fits	F115W filter response
jwst_niriss_f140m_trans.fits	F140M filter response
jwst_niriss_f150w_trans.fits	F150W filter response
jwst_niriss_f158m_trans.fits	F158M filter response
jwst_niriss_f200w_trans.fits	F200W filter response
jwst_niriss_f277w_trans.fits	F277W filter response
jwst_niriss_f356w_trans.fits	F356W filter response
jwst_niriss_f380m_trans.fits	F380M filter response
jwst_niriss_f430m_trans.fits	F430M filter response
jwst_niriss_f444w_trans.fits	F444W filter response
jwst_niriss_f480m_trans.fits	F480M filter response
jwst_niriss_gr150c-ordm1_disp.fits	GR150C order –1 dispersion
jwst_niriss_gr150c-ordm1_speceff.fits	GR150C order –1 response
jwst_niriss_gr150c-ordp1_disp.fits	GR150C order +1 dispersion
jwst_niriss_gr150c-ordp1_speceff.fits	GR150C order +1 response
jwst_niriss_gr150c-ordp2_disp.fits	GR150C order +2 dispersion

File Name	Description
jwst_niriss_gr150c-ordp2_speceff.fits	GR150C order +2 response
jwst_niriss_gr150c-ordp3_disp.fits	GR150C order +3 dispersion
jwst_niriss_gr150c-ordp3_speceff.fits	GR150C order +3 response
jwst_niriss_gr150r-ordm1_disp.fits	GR150R order −1 dispersion
jwst_niriss_gr150r-ordm1_speceff.fits	GR150R order −1 response
jwst_niriss_gr150r-ordp1_disp.fits	GR150R order +1 dispersion
jwst_niriss_gr150r-ordp1_speceff.fits	GR150R order +1 response
jwst_niriss_gr150r-ordp2_disp.fits	GR150R order +2 dispersion
jwst_niriss_gr150r-ordp2_speceff.fits	GR150R order +2 response
jwst_niriss_gr150r-ordp3_disp.fits	GR150R order +3 dispersion
jwst_niriss_gr150r-ordp3_speceff.fits	GR150R order +3 dispersion
jwst_niriss_gr700xd-ord1_disp.fits	GR700XD order +1 dispersion
jwst_niriss_gr700xd-ord1_speceff.fits	GR700XD order +1 response
jwst_niriss_gr700xd-ord2_disp.fits	GR700XD order +2 dispersion
jwst_niriss_gr700xd-ord2_speceff.fits	GR700XD order +2 response
jwst_niriss_gr700xd-ord3_disp.fits	GR700XD order +3 dispersion
jwst_niriss_gr700xd-ord3_speceff.fits	GR700XD order +3 response
jwst_niriss_h2rg_qe.fits	Detector quantum efficiency and photon yield functions
jwst_niriss_internaloptics-clear_throughput.fits	CLEAR element throughput
jwst_niriss_internaloptics-clearp_throughput.fits	CLEARP element throughput
jwst_niriss_internaloptics_throughput.fits	NIRISS pick-off mirror, three mirror assembly and camera three mirror assembly combined throughput
jwst_niriss_nrm_trans.fits	Fractional throughput of the non-redundant mask
jwst_telescope_ote_thruput.fits	The OTE throughput function

The filter response functions submitted to the ETC prior to launch are from the vendor measurements. For filters F090W, F115W, F140M, F150W, and F200W the original filter response was combined with the blocking filter response measured separately. For the GR150 grisms the ground measurements at Montreal were made on one particular grism from the set of flight candidates and these were assumed to apply to both the GR150R and GR150C grisms in the instrument. Thus, in the pre-flight ETC files the various GR150C and GR150R files are identical.

The detector response file gives both the assumed detector quantum efficiency function and the assumed photon yield function as separate columns in the FITS table. As noted above, these are average values from measurements of detectors in the same "family" that were NIRSpec candidates.

The various throughput values for the NIRISS components as well as the detector response functions are given on a common wavelength grid from 0.5 to 5.5 μm with a step of 0.001 μm.

2.1 The Revision Process

The revisions to the throughput files were carried out in an iterative sequence, attempting to isolate specific NIRISS components as much as possible. The initial set of revisions was made based upon the SOSS mode photometric calibration measurements because these cover the entire wavelength range from 0.6 to 2.85 μm in a single observation, and thus provide the best information about the changes required to the internal optics and detector values that are being used in the ETC. The inter-comparison of the order 1 results and the order 2 results gives some redundant information in the wavelength range from 0.8 to 1.4 μm that are covered by both orders, although the grism response is obviously different in the two cases. Comparison of orders 2 and 3 similarly provides some redundant information as well. At this stage some revisions were made to the NIRISS internal optics throughput function and the detector quantum efficiency values. The GR700XD blaze functions for orders 1, 2, and 3 where revised at this stage.

Once a reasonable set of revised response values were found for the SOSS mode, a cross-check was made with the WFSS mode since there is overlap in wavelength between the two modes. However, the overlap is limited and one has two additional independent elements involved, namely the grism and the filter. The cross-check was intended to make sure that the changes to the detector quantum efficiency and the internal optics did not produce unphysical estimates of the filter and WFSS GR150C/GR150R grism responses, namely that the values out would not need to be larger than 1.0 to match the observations.

After this cross-check a set of revisions were made to the imaging filter response values by looking at the imaging photometry results for one specific photometric standard star. Due to the lack of wavelength information a simple overall scaling was applied to the throughput function for each imaging filter. A check was made with the SOSS mode observations using the F277W filter at this stage, as that is the only one of the longer wavelength filters for which there is independent spectral information. For the shorter wavelength filters spectral information is available in the WFSS mode, but that information was not used to attempt to revise the relative shapes of the filter response functions.

Subsequently revisions were made to the GR150C/R grism response values in first and second order. Since each filter covers only a relatively small wavelength range these changes to the grism response were made based upon the combined data from all the six blocking filters used in the WFSS mode.

Finally, about 1 month after the NIRISS throughput revisions were finished a new OTE throughput file was provided by the telescopes group. The estimated changes to the telescope throughput were all relatively small. A final set of minor revisions were made to the internal optics and the quantum efficiency values to keep the product of these functions and the OTE response unchanged from what was used in the last iteration of the NIRISS throughput adjustments. The following sections provide the details of these steps in the order that the revisions were done.

There is some element of ad-hoc decision making that went into the various throughput revisions because some of the optical elements are common to all NIRISS observations and so cannot be explicitly measured as an individual component, and because in the cases of the other components that vary from observation to observation the amount of ground testing that went into the determination of the "starting point" functions were limited. In the process of making the revisions some assumptions were made about how the revised functions "should" look as a function of wavelength. Also, in some cases the signal-to-noise ratio of the measured values

was not as high as in other cases, so for these elements with lower quality measurements the ability to make detailed inferences as to the shape of the response function was limited by the input observations. The same end results could have been achieved with a different mixture of revisions between the various optical elements of NIRISS and the revisions to the detector quantum efficiency. Further revisions to the response functions may become necessary in the future as additional photometric observations are obtained. It is expected that any future revisions will be much smaller than the ones reported here.

3 Observations and Their Relation to the ETC Inputs

The on-sky measurements of the NIRISS photometric response were made in commissioning programs NIS-015/APT 1089 for WFSS photometric calibration, NIS-017/APT 1092 for SOSS photometric calibration, and NIS-020/APT 1094 for imaging photometric calibration. In each case one or more photometric standard stars selected from the CALSPEC pages (https://www.stsci.edu/hst/instrumentation/reference-data-for-calibration-and-tools/astronomical-catalogs/calspec; see Bohlin, Gordon and Tremblay (2014)) was observed. The output response in ADU/s, either the estimated total signal for the star corrected for aperture losses in imaging or the estimated total signal per pixel in the extracted spectrum in the spectral modes, was compared to the expected signal in Jansky from the CALSPEC model spectrum for the standard. The ratio of these two values is the response for the given filter or the given wavelength in the spectrum. This "conversion value" in units of Jansky/(ADU/s) was used as input for the derivation of the NIRISS response.

The derived quantities for the JWST data reduction pipeline were response values relating the NIRISS signal values in ADU/s to physical units. What units were used depended on the mode. For the imaging and WFSS modes the pipeline output units after the photometric calibration are surface brightness units, MJy/sr, so one needs to know the pixel area in steradians for the derivation of the photometric calibration. For the SOSS mode the pipeline units are flux density in MJy units. The response values were in all cases originally derived in Jy/(ADU/s) and these were then converted to the units (MJy/sr)/(ADU/s) or MJy/(ADU/s) as needed.

In the imaging case the "flux density" values used are averaged over the filter response function. The formula for the averaging is

$$\overline{F_\nu} = \frac{\int F_\nu \phi(\nu) d\nu/\nu}{\int \phi(\nu) d\nu/\nu} \quad (1)$$

where $\phi(\nu)$ is the "total photon conversion efficiency" function, the throughput of the OTE and the NIRISS internal components times the detector quantum efficiency function times the photon yield function. This is also the ratio of the number of electrons recorded at the NIRISS detector per photon reaching the JWST primary mirror from the source being observed at each frequency/wavelength. The value can be larger than 1 because the photon yield can be much larger than 1 at the shortest wavelengths covered by NIRISS. This photon weighted mean flux density value $\overline{F_\nu}$ needs to be calculated from the photon conversion efficiency function and the assumed standard star spectrum F_ν. This mean flux density value does not have an associated wavelength that can be identified. The only statement that can be made in general is that the object spectrum flux density will equal the photon weighted mean flux density at one or more wavelengths within the main part of the filter response function. This mean flux density is strictly proportional to the observed count rate at the detector independent of the spectral shape. The equivalent of equation (1) when expressed in terms of wavelength is

$$\bar{F}_\lambda = \frac{\int F_\lambda \lambda \phi(\lambda) d\lambda}{\int \lambda \phi(\lambda) d\lambda} \quad (2)$$

which is also strictly proportional to the observed count rate at the detector for any input spectrum (with the implicit assumption that the $\phi(\lambda)$ function is not missing some out-of-band response that would cause the calculated $\bar{F}_\nu$ value to no longer be proportional to the measured values).

For utility the photon weighted mean flux density is associated with the pivot wavelength calculated from

$$\lambda_p = \sqrt{\frac{\int_0^\infty \lambda \phi(\lambda) d\lambda}{\int_0^\infty \frac{1}{\lambda} \phi(\lambda) d\lambda}} \quad (3)$$

which then relates the mean flux density values in frequency and wavelength units in the usual manner. Nonetheless, the actual spectral flux density at the pivot wavelength may deviate significantly from these mean values. For spectra without absorption or emission lines the deviation will be small if the curvature is not very large over the main part of the filter response; for a linear spectrum there is no deviation between the two values.

Although the values of interest for imaging are the $\bar{F}_\nu$ values in Jansky, the inputs to the ETC are the $\phi(\lambda)$ values. One needs to convert from wavelength units to frequency units before carrying out the integration in equation (1).

As the photon weighted mean flux density is proportional to the count rate on the detector, for imaging mode the best comparison with the observations is to use the integrated count rate in electrons/s calculated from $\phi(\lambda)$ to compare with the observed count rate on the detector, rather than working with the conversion value for the pipeline. In the imaging case, we have no information about the shape of the $\phi(\lambda)$ function from the observations. Hence, the only practical correction that can be made in this case is an overall scaling of the current response function $\phi(\lambda)$ if a discrepancy between the predicted count rate and the observed count rate is seen. All these comparisons require that the NIRISS gain, the number of electrons per ADU on the detector, is known. For the work here the gain value is assumed to be 1.612 electrons/ADU; it should be noted that the gain value is difficult to measure accurately. We have no good estimate of the uncertainty in the gain value, nor can we determine with confidence that the gain is the same for all the detector pixels. The gain should be a function of the output amplifier electronics and be common to each of the four channels on the detector; ground measurements of the gain from several different data sets before the instrument integration and after in ISIM testing show a structure within the channel from the position of the amplifier feed across the detector along the slow scan direction. This is not understood. If this variation is due to the measurement uncertainties, then these are of order 5%; but it would be unusual for the calculated gain variation over the detector to be the same when the illumination pattern was different in the various measurements. The measurements of the channel gain values made by Teledyne in units of μV/electron show only much smaller variations from channel to channel. The conversion of output voltage to the signal in ADU should be the same for all four channels. These considerations would mean that the gain in electron/ADU should be very similar for the four channels.

For the imaging case the count rate estimates were taken from a python program written by the author for general magnitude and count-rate simulations of the NIRISS filters along with those of the other JWST instruments and a wide variety of ground-based and space-based filters, with emphasis on the infrared wavelengths. This code has been validated against calculations using the synphot package made by Paul Goudfrooij in the case of the NIRISS filters. During commissioning discrepancies were noted in the count rate predictions from the NIRISS team codes and those from the ETC. Since the same throughput files were used for all these calculations the discrepancies were not understood at that time. This was eventually traced to differences in the PSF footprints used in the ETC calculations compared to the calculations in the NIRISS team codes (Goudfrooij et al. 2022). In the work here calculations in the author's codes are used exclusively for comparison with the on-sky imaging observations without any attempt to make comparisons with the ETC predictions.

3.1 Relation of Conversion Values to the NIRISS Response

The spectral conversion factor in Jansky/(ADU/s), denoted as C(λ) here, is a direct measure of the ϕ(λ) function. It can be expressed as

$$C(\lambda) = \frac{h\upsilon g}{10^{-26}\Delta\upsilon A\phi(\upsilon)}. \quad (4)$$

In equation (4) h is Planck's constant, A is the JWST primary mirror area, g is the NIRISS detector gain, Δν is the frequency interval per pixel in the spectrum, and ν is the frequency associated with the wavelength of interest. The right-hand side of equation (4) is expressed in frequency units because the output flux density is in frequency units. The factor of 10^{-26} is the conversion from W/m^2/Hz to Jansky. The A value is taken to be 25.4009 m^2. Note from equation (4) that higher ϕ(λ) values give lower C(λ) values: a smaller flux density in Jansky corresponds to 1 ADU/s when the ϕ(λ) value is increased.

One could write an equivalent equation to equation (4) for imaging where ϕ(λ) is replaced by a mean value of ϕ over the filter response and C(λ) just becomes a mean C value. Since the simulated and observed count rates are being directly compared rather than the conversion factors this is not needed here.

For the comparison with the ETC throughput values equation (4) was rearranged to the form that converts C(λ) to ϕ(λ), since it involves a group of constants along with the pixel dispersion of the spectroscopy mode

$$\phi(\lambda) = \frac{h\upsilon g}{10^{-26}\Delta\upsilon AC(\lambda)}. \quad (5)$$

The input values being used for the throughput adjustments are: the C(λ) values for the SOSS mode order 1, 2, and 3; the C(λ) values for the two WFSS grisms in order 1; the C(λ) values for the two WFSS grisms in order 2 for the F090W filter only (since that is only case where order 2 is used for science); and finally the imaging count rate values for standard LDS 749B from program NIS-020. This was the order of precedence in the adjustments since the GR700XD grism gives the largest wavelength coverage and is of the most use in determining the NIRISS detector response. There is of course some interplay between the WFSS measurements and the imaging throughput values since the imaging filters are used as blockers for the WFSS observations. Also, as noted in the Introduction the OTE throughput, NIRISS

internal optics, and the detector response are common to all NIRISS observations and cannot be separated by the on-sky observations.

4 Throughput Adjustments from the SOSS Photometric Measurements

The SOSS photometric measurements were made using the standard star BD+60°1753. This is an A0V star with a mild Am character so that it is assigned spectral type A1V from the metallic lines in the optical spectrum. The CALSPEC model spectrum as well as the STIS spectrum over the optical wavelengths to roughly 1 μm show only the broad hydrogen lines over the NIRISS wavelength range at the GR700XD resolution. The ratio of the flux density in Jansky to the observed spectral count rates was derived using an extracted spectrum with an aperture width of 40 pixels, ±20 pixels from the estimated centre of the trace along the detector x direction. The spectral extraction was done using a simple box extraction initially, while later an extraction with the "Alogithim to Treat Order Contamination" (ATOCA) software (Darveau-Bernier et al., 2022) was applied instead. For the initial comparisons no aperture correction was applied to the spectral values. Spectra were extracted for orders 1, 2, and 3 with the CLEAR element in the filter wheel, and just for order 1 with the F277W filter as a blocker. For each order a smooth polynomial function of wavelength was fit to the observed conversion values. The functions then converted to $\phi(\lambda)$ values with the observed average dispersion values from each order. There is a small change in dispersion with wavelength in the GR700XD grism orders, but the effect was neglected here. The $\phi(\lambda)$ values that result are shown in Figure 1. We were already aware at this point that the peak count rates observed in the GR700XD/CLEAR SOSS mode were significantly larger than expected from the ETC calculations in all three orders. To compare with the observed $\phi(\lambda)$ estimates, the values for the various ETC throughput factors and the detector response values were multiplied together to get the simulated $\phi(\lambda)$ function. This is also shown in Figure 1 for the four combinations of interest. Each of these curves is the product of either four or five throughput functions: the OTE throughput, the NIRISS internal optics, the detector response, and finally the grism response for the order of concern plus the filter response in the GR700XD/F277W case. Both the CLEAR and F277W response functions provide information on the order 1 response. In these measurements the relative response between F277W and CLEAR was consistent with the filter response curve for the F277W filter, so no revisions were made based on the F277W data.

4.1 Changes to the Internal Optics Throughput Estimate

Figure 1 shows significant discrepancies between the observed values and the predicted values for wavelengths less than 2.1 μm. At longer wavelengths the agreement is better. There is an obvious change in response at 2 to 2.1 μm in the simulated $\phi(\lambda)$ values that is not indicated in the observed values. Examination of the different component response values in the ETC throughput files showed that this change at about 2 μm is due to the internal optics throughput file, as is shown in Figure 2 where the NIRISS internal optics throughput function and the OTE throughput function are plotted together, along with the F200W throughput function since this change in throughput would also affect the imaging and WFSS observations using the F200W filter.

The various reflective surfaces in NIRISS that produce the combined internal optics response are seven gold-coated surfaces. Individually they should be similar in shape to the OTE response from its three gold-coated surfaces. The decline in the NIRISS internal optics response at 2 to 2.1 μm is clearly the cause of the odd transition seen in Figure 1. The reason

for this decline in the function in the 2017 ETC input file is not known.

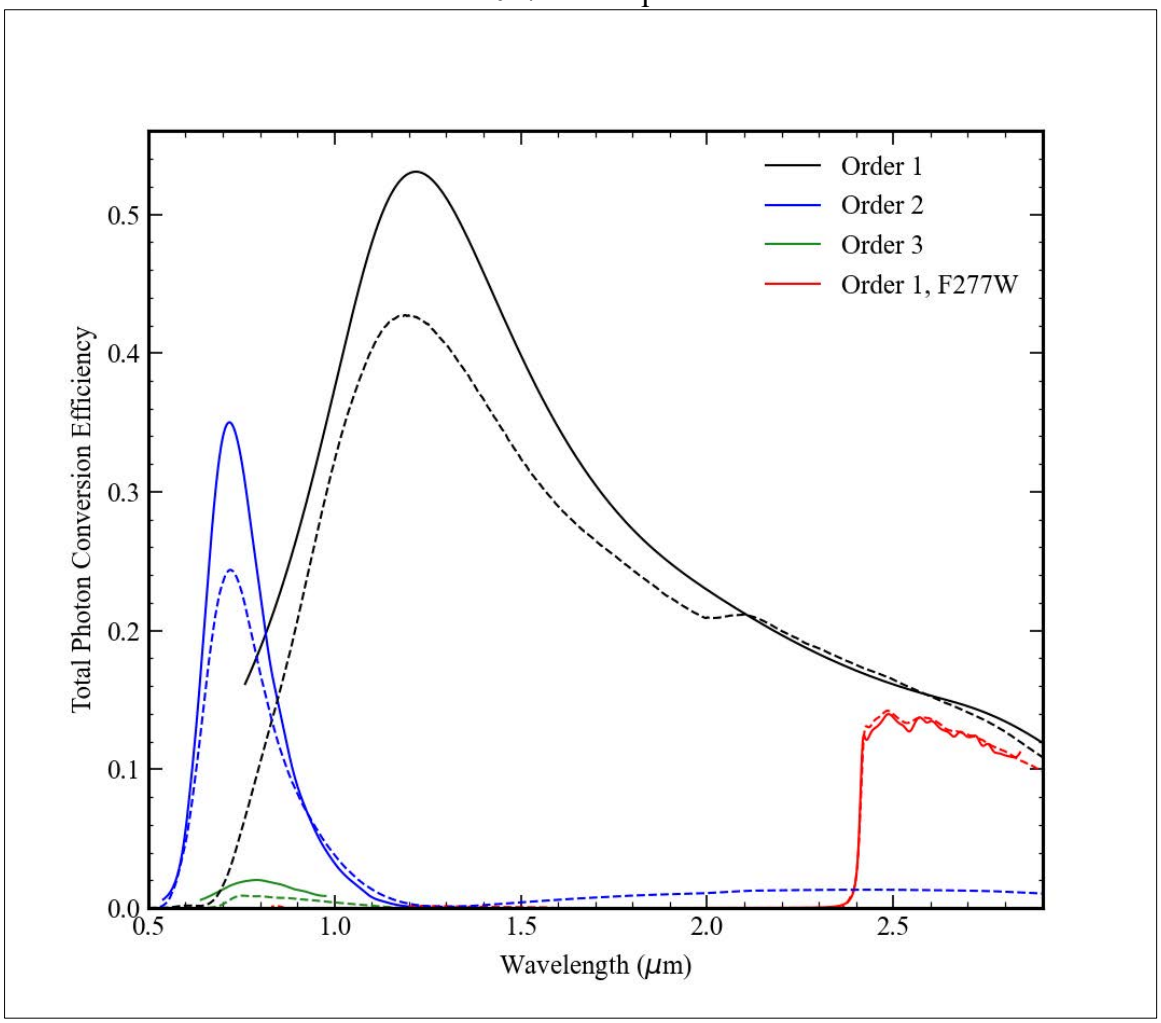

Figure 1: Comparison of the measured photon conversion efficiency derived from the conversion function (solid lines) to the pre-flight ETC predictions (dashed lines) for the SOSS mode observations.

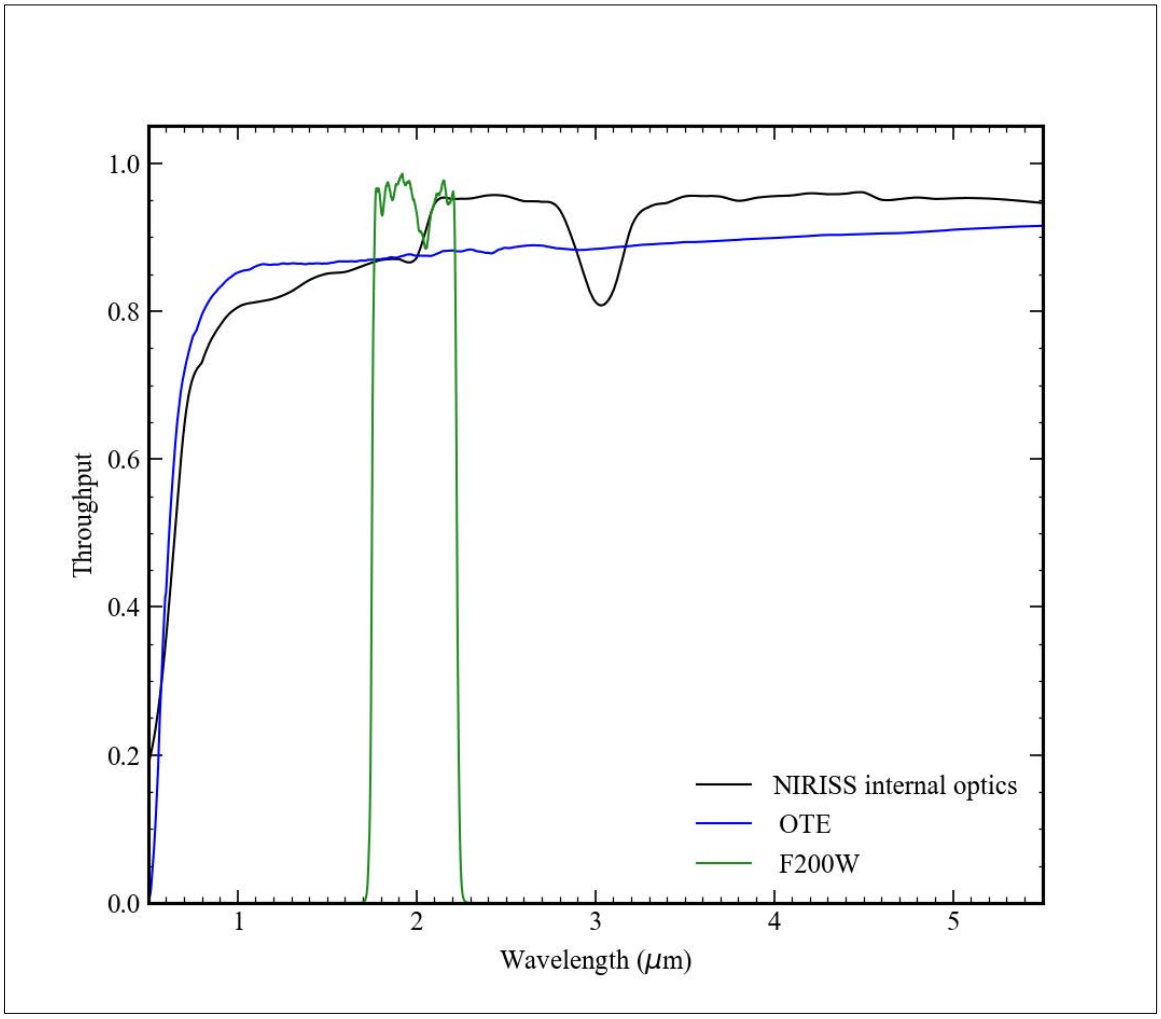

Figure 2: Plot of the OTE and NIRISS internal optics response functions from the 2017 delivery, along with the F200W response function for comparison.

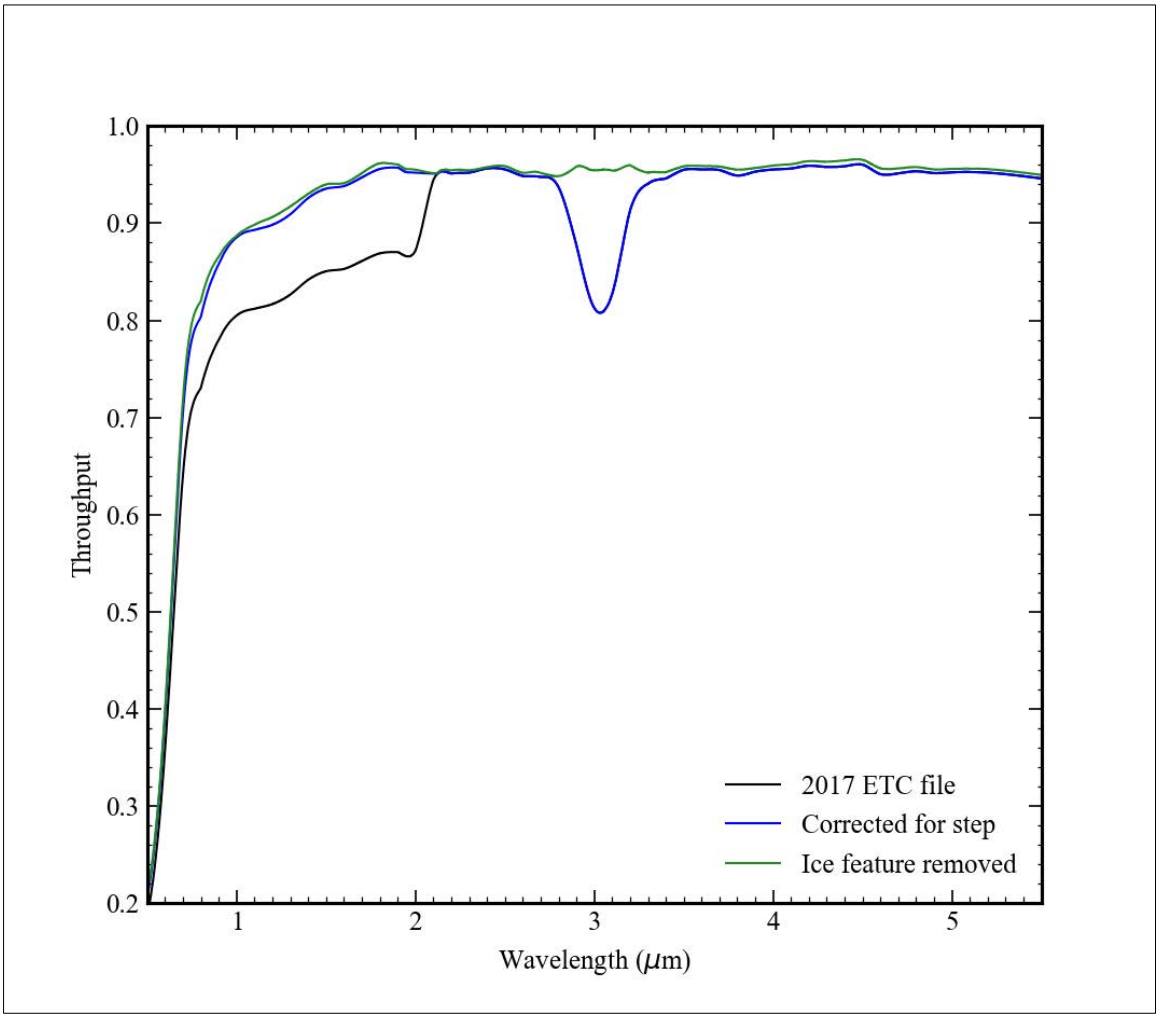

Figure 3: Corrections to the internal optics throughput values.

Another thing that is prominent in Figure 2 is the water ice contamination feature at 3.1 μm. No equivalent feature is present in the OTE throughput curve. We have no direct NIRISS measurements that can probe the water ice feature with any confidence, since the SOSS measurements cut out at 2.85 μm, just on the edge of the feature. Spectral measurements by NIRCam and NIRSpec over the 3 μm region showed no sign of any water ice absorption. It is assumed that NIRISS also has no water ice absorption based on those measurements. As a result, the internal optics throughput values were changed to first remove the step at 2 μm and then to remove the water ice feature. Figure 3 shows the result of the corrections.

After the removal of the step function in the internal optics response the comparison of the observed and simulated photon conversion values looks much better around 2 μm. This is shown in Figure 4. One sees that the discrepancies between the prediction and the measurements now become significant at wavelengths shorter than 1.8 μm, but both functions are smooth as expected. The revised internal optics throughput was used in all subsequent comparisons with the observed response values, and there was no indication in the WFSS observations using the F200W filter that the original step down in the internal response within the F200W filter is present.

For the observed points in Figure 4 one sees specific wavelengths where the data points go up and then down over a small wavelength range. Each of these features is seen at the wavelength of one of the hydrogen absorption lines in the spectrum. This indicates that either the line profiles from the model is different from those in the observed spectra or that there is a small wavelength discrepancy between the observed spectrum and the model spectrum at the line positions (and presumably for the wavelengths in between), or both. The regions of the hydrogen lines were excluded from the fitting of the function as needed to produce a smooth fit.

5 Quantum Efficiency Revisions

The large discrepancies in the response seen in Figure 4 at short wavelengths were assumed to be primarily due to the detector quantum efficiency, both because that is the most uncertain part of the NIRISS response and because attributing this to the grism response would produce unrealistically high response values. Although the peak of the observed total photon conversion efficiency function in GR700XD order 1 is only about 0.54, this includes an aperture blocking factor of about 0.663 for the grism in the NIRISS pupil wheel so the combined other throughput values peak at about 0.81. This blocking factor might be slightly in error, but one clearly cannot accommodate a 20% increase in the GR700XD order 1 blaze response without requiring unphyscally large throughput values for the grism. The peak GR700XD grism response is expected to be about 0.8 due to the anti-reflective coating.

The photon yield function for the NIRISS detector was not measured in the ground testing. The function that was delivered to the ETC is a mean photon yield curve based on measurements of the NIRSpec detector candidates made at Goddard Space Flight Center. Those NIRSpec candidate detectors were manufactured in the same group as the NIRISS and FGS flight detectors, so it is assumed that the mean photon yield curve from these detectors is representative of the NIRISS detector yield. In the absence of available measurements, the photon yield was treated as fixed and would only have been considered for revision if there was an obvious issue with the detector quantum efficiency being higher than 1 at the shorter wavelengths. While it is true that we cannot measure the detector quantum efficiency separately from the photon yield, only the quantum efficiency was revised to match the on-orbit observations.

A small initial shift of the GR700XD order 1 blaze function was undertaken first on the assumption that the small peak shift seen in Figure 4 was due to the grism and not due to the detector. The detector response peaks are expected to be at somewhat shorter wavelengths than the peak of the overall response. An offset of +0.01 μm in the entire order 1 blaze function produced a better match to the observed values.

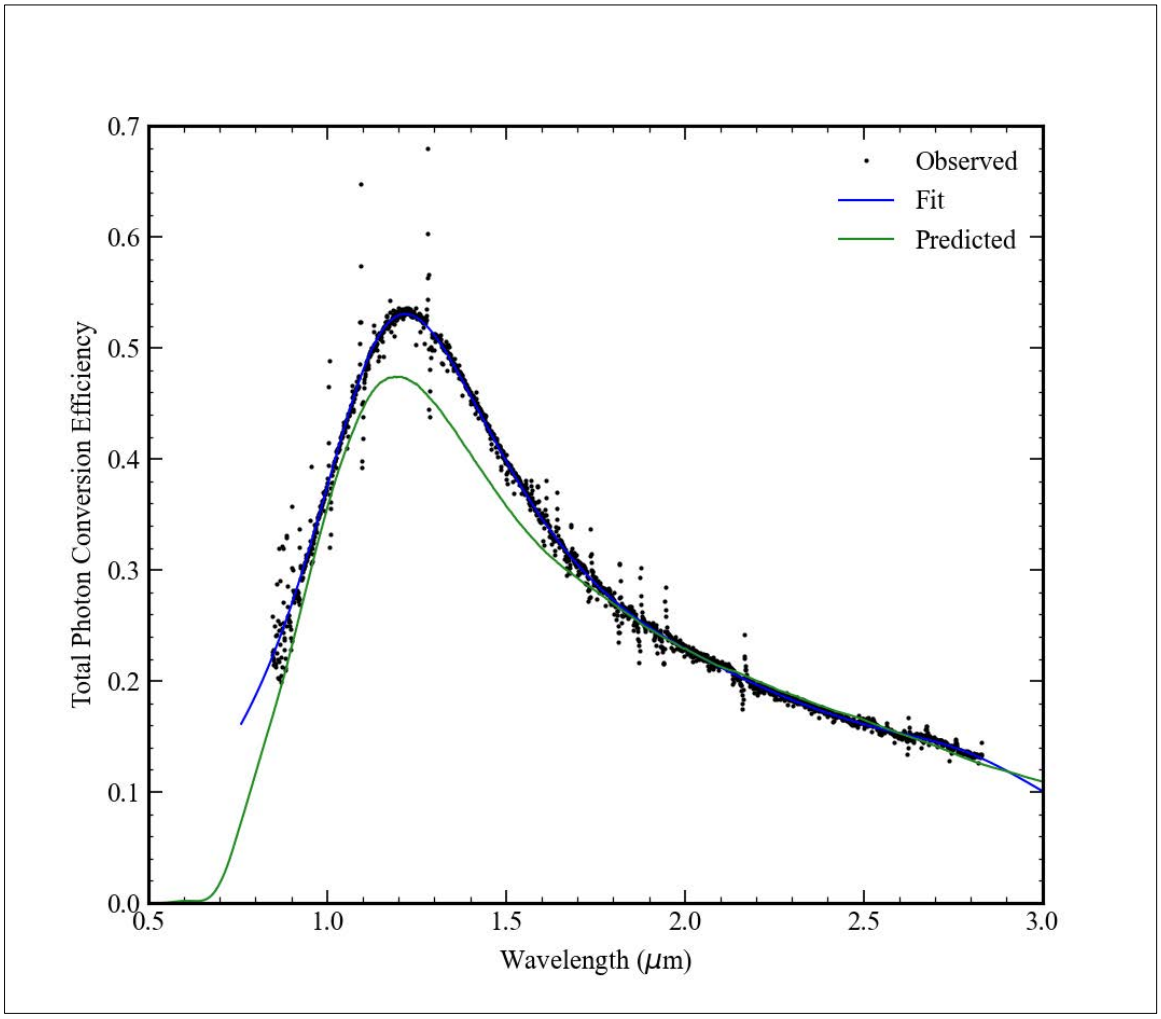

Figure 4: Comparison of the GR700XD/CLEAR order 1 total photon conversion efficiency values from the observed conversion values (black circles) and the fitting function from those values (blue line) with the prediction from the ETC throughput values after the internal optics correction in Figure 3 (green curve).

To estimate the changes required for the detector quantum efficiency the ratio of the observed to the predicted total photon conversion efficiency values was calculated for order 1 and order 2, and these ratio values were then used to scale the quantum efficiency function. This lead to the prediction of the peak shapes for two peaks that are expected in the quantum efficiency values. For order 2 the resulting peak was significantly higher than 1.0, which would require a change to the photon yield function if I wanted to match the values solely by changing the assumed detector properties. In that case, it was assumed that the order 2 response observed was higher than predicted, and the ratio function was adjusted to keep the two quantum efficiency peaks below 1.0. Those values were then cross-checked with the order 1 value of the GR150 grisms (of the WFSS mode) to ensure that a reasonable result was obtained, and it appeared that the three grisms were in reasonable agreement with such a change in the detector quantum efficiency, and with no change in the photon yield function. There is some wavelength overlap between GR700XD order 1 and order 2 that also was useful in constraining the shape of the quantum efficiency curve. The end result of this iterative process is shown in Figure 5. In this work no comparison was made with the sparse Teledyne measurements of the detector quantum efficiency, because these were thought to be of

relatively low quality as they could not be fit with the expected anti-reflective coating function provided by Teledyne. In the end, though, the output values agree fairly well with the Teledyne measurements at the shorter wavelengths.

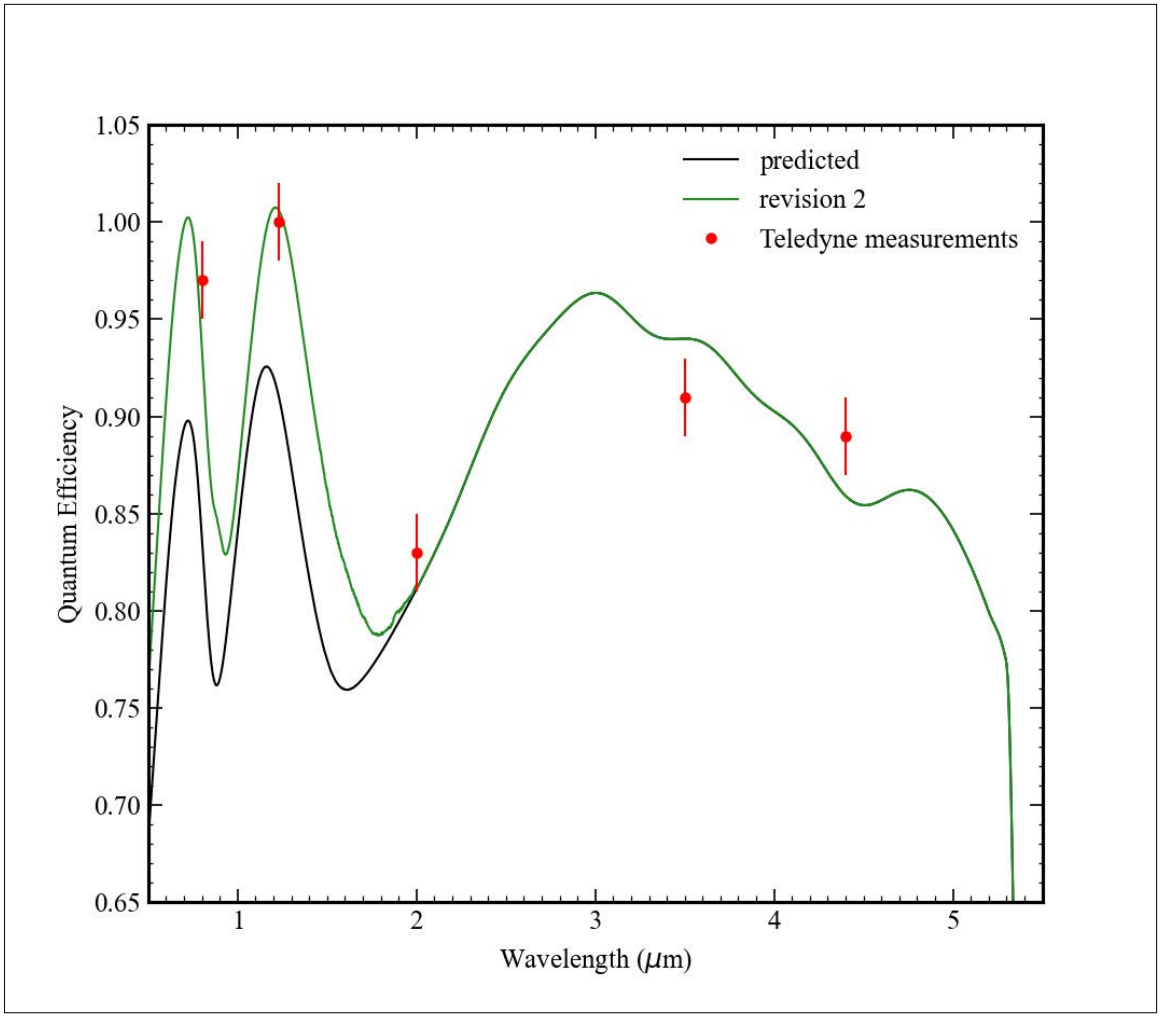

Figure 5: The mean quantum efficiency function from the 2017 ETC inputs is plotted along with the revision from the on-sky SOSS data and the original Teledyne measurements. No changes were made to the function at wavelengths longer than 2 μm.

One issue with the Teledyne measurements is that they have been corrected for the photon yield function, but exactly what corrections were assumed were not recorded in the data package for the NIRISS detector. At this late date it is unlikely that we can get these values from the people at Teledyne. This is only an issue for the two short wavelength points. For reference, the assumed photon yield values currently in the ETC are 1.4117 at 0.8 μm and 1.1617 at 1.23 μm. The values used by Teledyne to correct the measurements in the data package should be similar to these values, but offsets of a few percent cannot be ruled out.

The longer wavelength shape of the quantum efficiency curve may well be incorrect; the discrete bumps at about 3.56 and 4.77 microns are probably not real since the individual quantum efficiency curves from the NIRSpec candidate detectors did not show this type of feature. However, with no spectroscopic measurements available, it is difficult to determine

what changes (if any) should be made at wavelengths beyond 3 μm.

The revised quantum efficiency curve peaks at 1.01 around 1.2 μm. This was understood to be unphysical. The entire curve needs to be reduced slightly. This work was done in early June when it was not known how the assumed OTE throughput would be revised for the on-orbit performance. Since any increase in the assumed OTE throughput would need to be compensated by changes to either the assumed internal optics throughput or the assumed detector response, at this stage I did not worry about a small offset of the assumed quantum efficiency values, but left this revision to be done later when the new OTE throughput function was available. The final adjustment is described in Section 11.

6 GR700XD Grism Response Changes

Once the changes had been made to the estimated internal optics throughput and the estimated quantum efficiency function, the next step was to make changes to the GR700XD grism response functions to match the simulated photon conversion efficiency values to the measured ones. At this point I needed some type of aperture correction for the SOSS observations. In the initial revisions described in the previous sections I was working with the SOSS spectral extractions without any aperture corrections, on the assumption that these corrections are small compared to the other components of the problem that needed to be addressed initially. For the detailed grism response revisions, though, I could no longer neglect the aperture corrections in making the comparisons with the simulated values. Also, at this point the spectral extraction procedure used in the pipeline was changed to use ATOCA which produced some change in the input values before any aperture correction at the few percent level.

6.1. SOSS Aperture Corrections

Deriving the GR700XD aperture corrections presents a problem because of the nature of the SOSS observations. The GR700XD grism incorporates a weak cylindrical lens to disperse the spectral point spread function (PSF) so as to allow brighter objects to be observed. The monochromatic PSF for the GR700XD grism was observed at a small number of discrete wavelengths during the ground testing, but these observations did not have sufficient signal-to-noise (S/N) ratios to allow an aperture correction to be defined. For on-sky measurements most of the commissioning data was taken in the SUBSTRIP256 or SUBSTRIP96 sub-arrays. It appears that the full extent of the PSF is significantly larger than the 256 pixel cross-dispersion extent of the SUBSTRIP256 sub-array that is normally used for this mode. Low level signal is seen out to at least 200 pixels on either side from the trace centre when full-frame spectral images are taken in SOSS mode. The usual position of the SOSS spectrum near the top of the detector precludes measurements of the low-level signal in one direction from the trace. The WebbPSF code does not do a good job in predicting the extended, low-level structure in the observed PSF and so cannot be used to estimate the aperture corrections in this case.

There is one available commissioning observation where the SOSS spectrum was displaced to the center of the full frame array, which was done in program NIS-018 the SOSS wavelength calibration program. Observation 2 in the program, APT 1092, displaced the target by 67.1 arc-seconds down in the y direction, nominally about 1020 NIRISS pixels, in the output image from the usual position at the top of the detector. Full frame images were taken with the grism in the beam for the CLEAR and F277W cases. The target of the observation was the M-type main sequence star TWA 33. The rate image from the pipeline for that

exposure is shown in Figure 6 below. There is clearly a lot of contamination in the image from faint sources. While these are not generally of concern for the wavelength calibration of SOSS mode, they are a concern for any type of signal measurements at the few percent level.

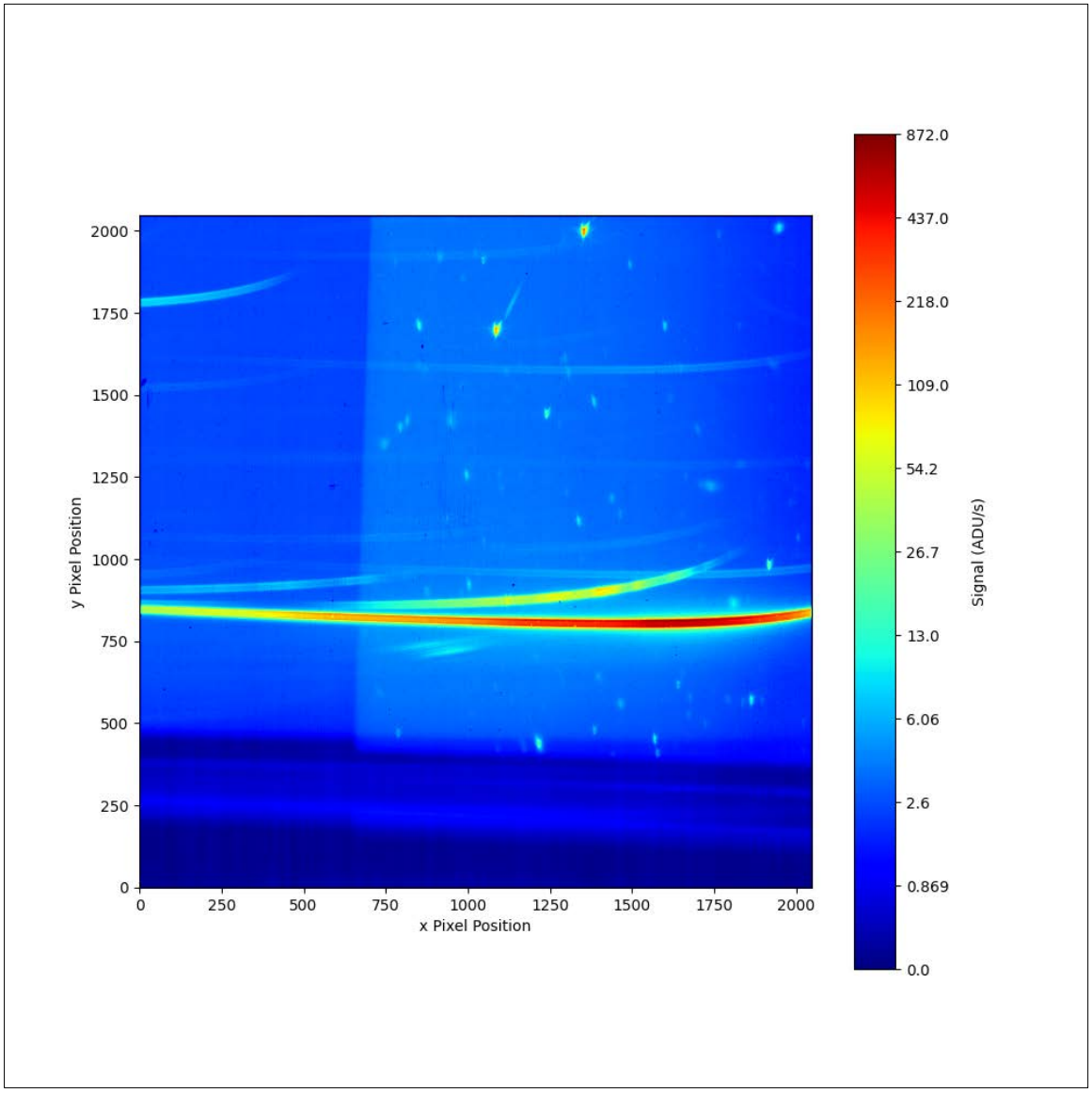

Figure 6: The output rate image from the JWST pipeline, in logarithmic scaling, for file jw01092002001_02101_00001_nis_rate.fits. The spectrum of the target TWA 33 is seen at roughly y pixel value 850.

The deblending code in the SOSS spectrum extraction code ATOCA was not working when the commissioning analysis was done. If it were working it would at least allow the order 1, order 2, and order 3 spectra to be separated for TWA 33. In the absence of this sort of deblending code the only crude measurement that could be made of the aperture corrections was to take the signal in the standard aperture, ±20 pixels from the trace position, and compare it with the signal in the range ±200 pixels from the trace position. This ratio would give a fairly good approximation to the aperture correction for an isolated source if the different spectral orders could be disentangled.

Under the circumstances the best that could be done was to make this calculation with the CLEAR and F277W observations at this position and look for places in the image where the contamination is limited. Figure 7 shows a plot of the resulting values across the image. The extractions are made using strips of pixels along the y direction with no tilt. The wavelength direction is actually slightly tilted away from the y axis.

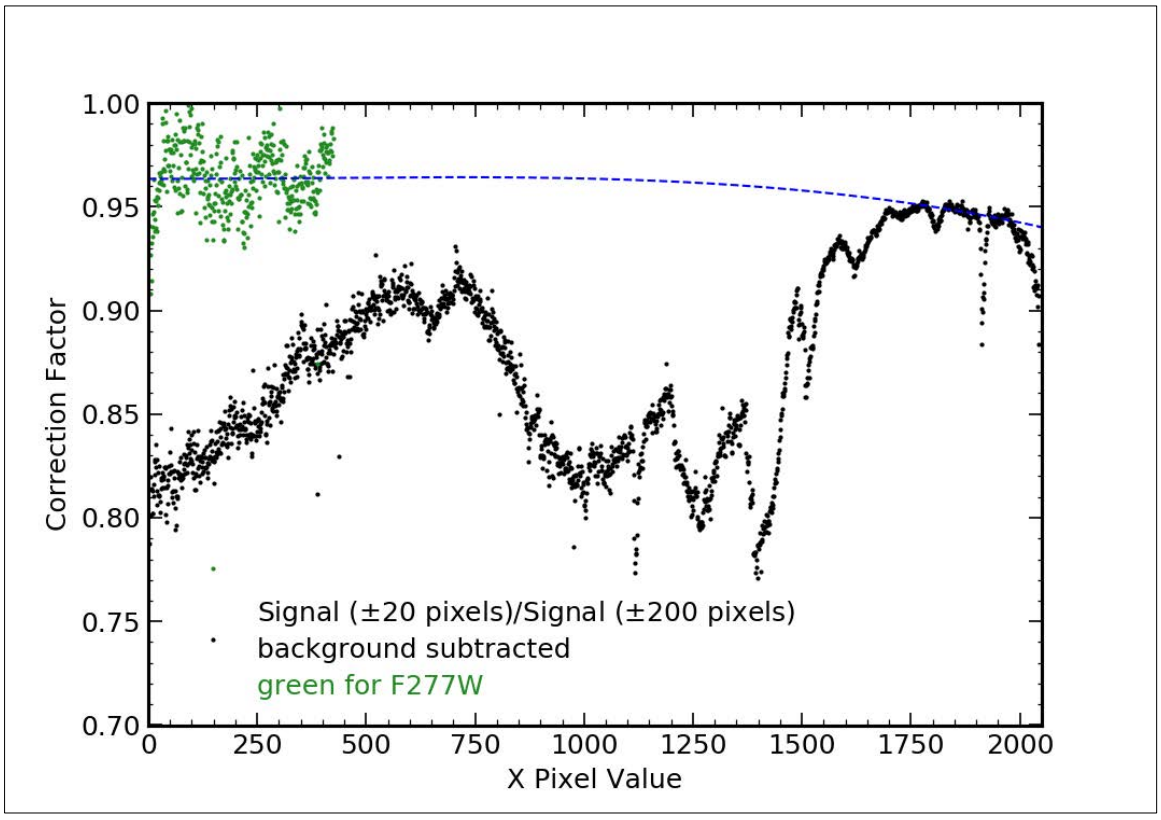

Figure 7: The signal ratio for the standard SOSS extraction aperture to a 10 times larger aperture derived from program 01092 observation 2 in first order. The extraction apertures are along the pixel y direction. There is clearly significant contamination from other orders and from sources other than the target TWA 33. The dashed line shows an order 3 polynomial fit to the upper envelope of the CLEAR points at pixels 1800 to 2024 along with the F277W values where contamination and overlap are much less of an issue.

Examination of the F277W image shows that there is little contamination, but the overall S/N is much lower than in the CLEAR case. A simple order 3 polynomial fit was made to the F277W average ratio value along with some narrow regions in the CLEAR ratio value to make a smooth aperture fraction function. There is no part of the order 1 spectrum that is not subject to some contamination even x positions larger than 1800, since there is a faint first order spectrum seen about 150 up from the TWA 33 spectrum. This contamination spectrum is from object 2MASS 17244630+6025483, estimated to be a field K5V star from the available Gaia and 2MASS photometry. The SOSS spectrum of this star is about 100 times fainter than the spectrum of TWA 33.

The inverse of the correction factor from the fit function was used to correct the observed signal values for aperture effects. The correction function was extrapolated to shorter wavelengths and applied to orders 2 and 3, although we do not have measurements to support this extrapolation. Unfortunately, star TWA 33 is relatively cool and as a result the order 3 spectrum is very faint, so it was not practical to attempt to make any measurements for short

wavelengths. In future cycles it may be necessary to observe a target that will allow a better measurement of the SOSS aperture corrections.

6.1. GR700XD Blaze Corrections

Having obtained the aperture correction function this was applied to the observed signal values from the ATOCA extraction, and then these were converted to total photon conversion efficiency values. In each order a new polynomial fit was made to produce a smooth response curve, similar to what is seen in Figure 4 above. For each order the ratio of the fit to the observed photon conversion efficiency values to the predicted values was used to correct the grism blaze function. This necessarily involved some extrapolation beyond the observed wavelengths in the SOSS data for the orders; at long wavelengths the ratio value was simply kept fixed at the last measured value since these values were close to 1.0, while at short wavelengths a (somewhat arbitrary) extrapolation was used with a floor value of 1.0 at shorter wavelengths. The magnitude of the corrections required was somewhat larger for order 2 than for order 1.

The GR700XD order 3 was a special case. Comparison of the predicted blaze function, which peaked at about 0.55 μm, with the observed response, which peaks at about 0.75 μm, showed that the prediction was far off of the real response. In that case the ratio of the observed to predicted response becomes large and in fact has problems where the predicted blaze function goes to zero within the wavelength range of the observed response. Due to this bad match in wavelength, the observed order 3 response was divided by the simulated response for all the other components except the grism response to provide an estimate of the grism response. This curve was used as a starting point rather than the grism response function that had been delivered to the ETC from the ground testing. The original order 3 blaze function was produced from the assumed order 2 blaze function using the blaze equation; apparently this was a bad approximation for the GR700XD grism.

Figure 8 shows the match of the revised total photon conversion efficiency functions from the ETC input files to the observed values for the different SOSS orders and blocking elements. Figure 9 shows the revised blaze functions for the three orders used to obtain these results. The transition in the order 1 blaze function between the end of the observed values at 2.85 μm and the long wavelength values beyond 3 μm is visible in Figure 9 as a bump on the response curve. This could in principle be revised to improve the transition to something smoother. It is not clear how this should be done in the absence of suitable observations so it was left as is for now. In any case, the values beyond 2.85 μm are not used in the ETC since we have no science observations at such wavelengths so the point is moot. The order 2 values at wavelengths longer than the minimum are inaccurate because the order contamination was not working in ATOCA for the extraction, so those values were ignored in the revisions.

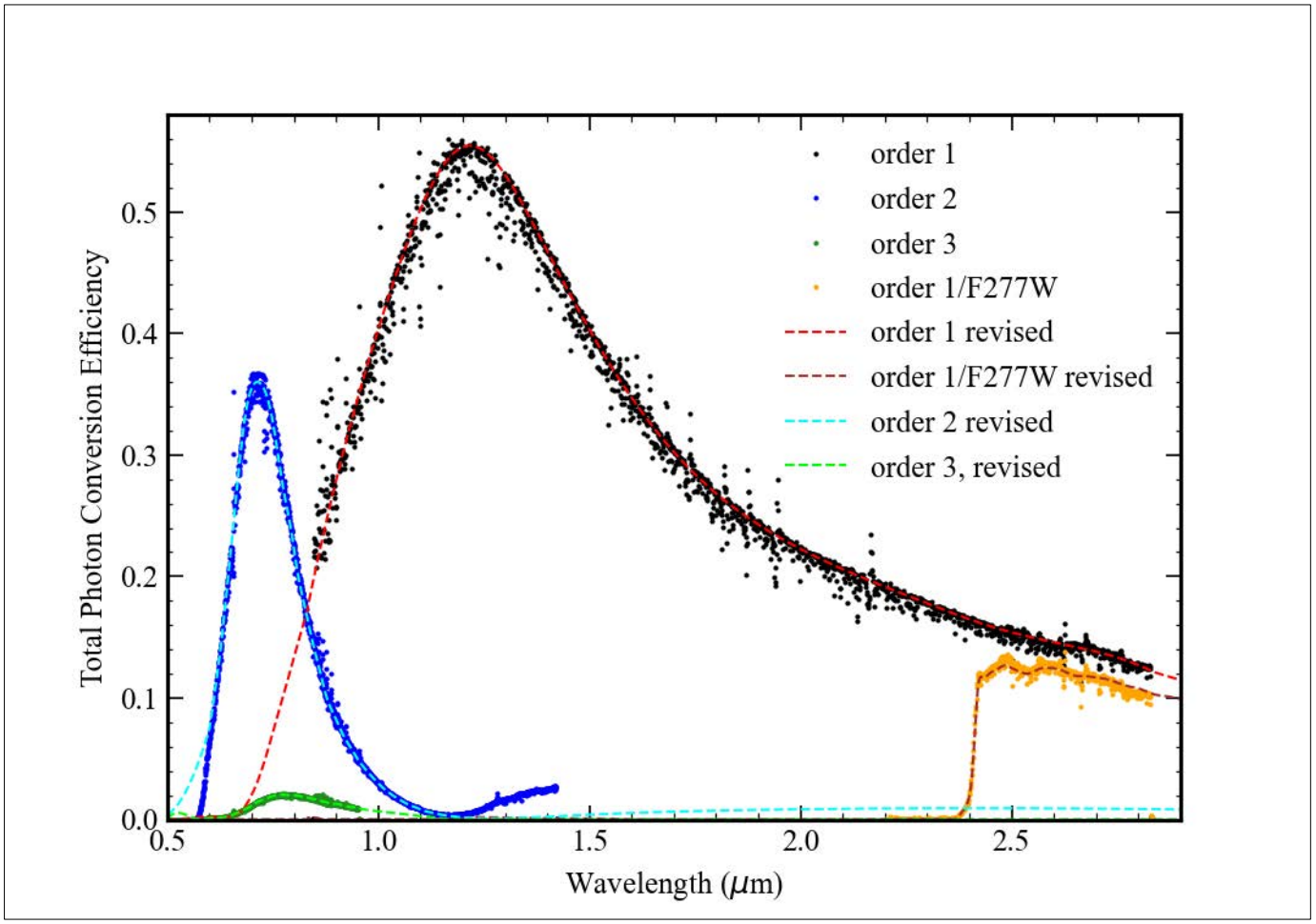

Figure 8: The revised total photon conversion efficiency values after adjustments of the GR700XD blaze functions (dashed curves) compared with the values derived from the extracted spectrum using ATOCA (points).

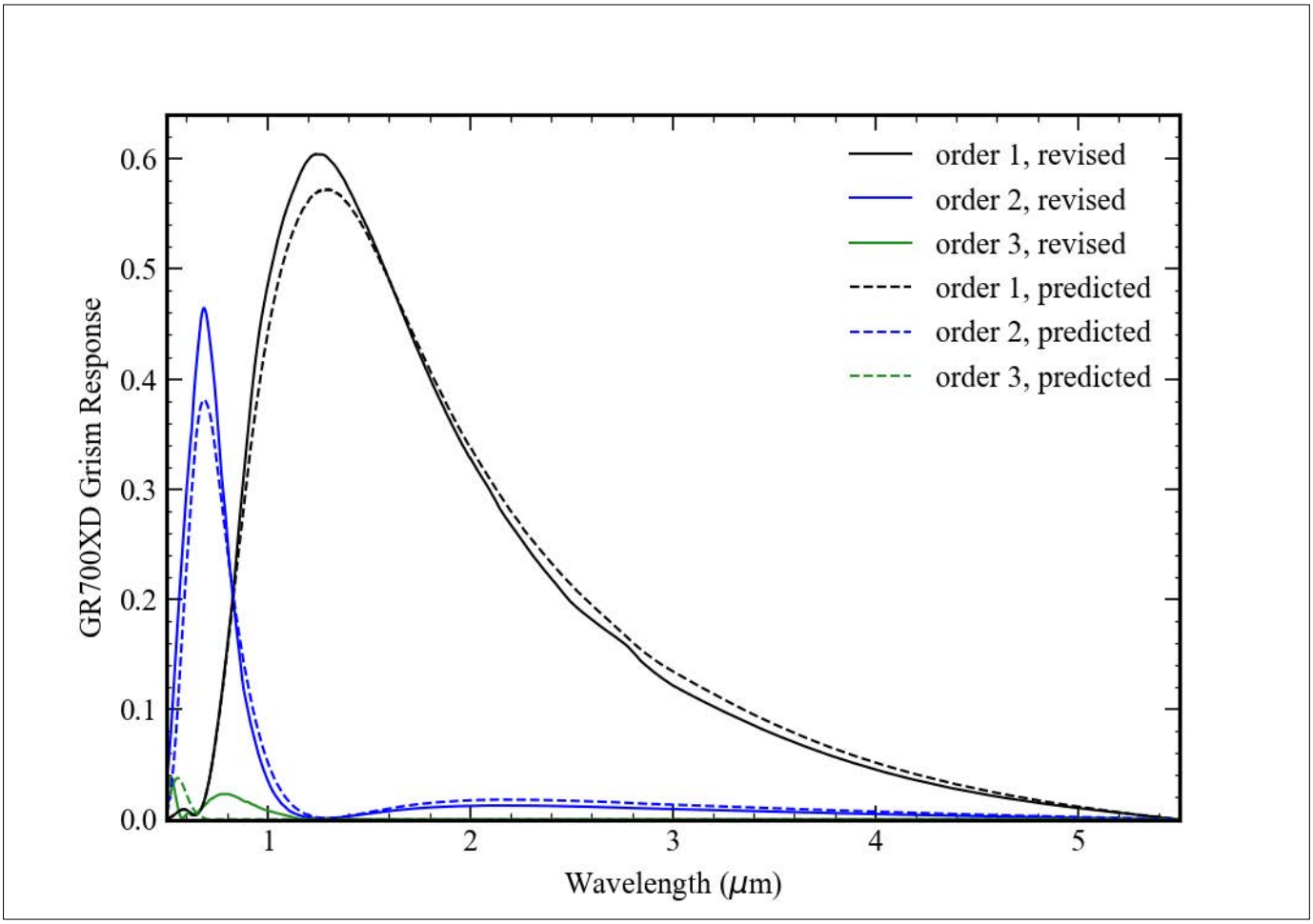

Figure 9: The resulting GR700XD response functions for orders 1, 2, and 3 after matching to the observed total photon efficiency values.

One also sees in Figure 9 that the original order 3 response (the green dashed curve) is almost entirely disjointed from the on-orbit values (the solid green curve). There are small changes to the peak wavelengths for orders 1 and 2 from the ratio correction, but mostly the changes produce an increase in the overall amplitude. For order 3 the peak response is somewhat lower than was originally predicted and the width of the peak is somewhat larger than originally predicted, but the main difference is the large wavelength shift.

Also of note in Figure 8 is that the F277W response as measured matches closely the predicted values from the throughput files. The relative response between GR700XD/CLEAR and GR700XD/F277W depends only on the F277W response function since CLEAR is empty and it is certain that it has a transmission of 1.0 at all wavelengths. Given that the throughput revisions match the data closely in both cases, the filter response of F277W is quite accurately described by the filter transmission function over the part of the response that is measured in this mode.

7 Imaging Throughput Comparisons

Before working on the WFSS results a comparison was made of the predicted count rates and the observed count rates for the photometric standard LDS 749B from the imaging photometric calibration program NIS-020. All the changes in the NIRISS response values

described previously were used in the calculation of the predicted count rates. The results of this comparison are listed in Table 2 below. The weighted mean count rates from all the LDS 749B observations in the NIS-020 program are used for comparison with the simulated values.

Table 2: Comparison of the simulated and observed total count rates for the NIS-020 observations of LDS 749B.

Filter	Count Rate (ADU/s)	Simulated Count Rate	Ratio Observed/Simulated
F090W	113626±2756	112979.5	1.006±0.024
F115W	84632±1847	83372.37	1.015±0.022
F140M	27074±156	26858.21	1.008±0.006
F150W	50101±393	50020.77	1.002±0.008
F158M	22617±143	22868.12	0.989±0.006
F200W	28766±307	28818.18	0.998±0.011
F277W	16845±112	15318.63	1.100±0.007
F356W	10584±464	9839.73	1.075±0.047
F380M	1921±80	1781.68	1.078±0.044
F430M	1236±33	1141.89	1.082±0.029
F444W	6697±216	5971.20	1.122±0.036
F480M	1117±36	1020.22	1.095±0.035

For the short wavelength filters the ratios of the observed and predicted counts are all close to 1.0. The F158M ratio is about 2 sigma low, the other values deviate less than this. The average of the six values for the short wavelength filters is almost exactly 1.0.

The situation for the longer wavelength filters is different. All the values are somewhat larger than 1.0 and do not show a clear trend with wavelength. The values are probably an indication that the detector quantum efficiency is low for these wavelengths, particularly if one assumes that the level of discrepancy seen for the short wavelength filter tells us that maximum level of uncertainty in the filter throughput measurements is roughly 1%. The one concern here is that the F277W filter has a 10% discrepancy with the prediction, whereas the SOSS observations with the F277W filter used as a blocker show good relative agreement with the CLEAR case. Unless there is some large out-of-band long wavelength leak in the F277W filter, which will be tested in cycle1 calibration by observing an asteroid through the imaging filters, this suggests that the quantum efficiency should be revised and the SOSS order 1 response at these wavelengths also revised in the opposite relative sense to keep the product constant and thus preserve the match seen in Figure 8 above. Whether so large a change can be accommodated needs some investigation.

8 Long Wavelength Quantum Efficiency Revision

Using the ratio values for the long wavelength filters, and assuming that these apply at the pivot wavelength, a smooth function was fit to the ratio values along with end points set to 1.0 at 2.46 and 5.26 μm. The long wavelength end point is somewhat arbitrary, but is beyond the F444W and F480M main response. The short wavelength point was chosen to be just shortward of the F277W main response. As noted in section 5 the round of QE revisions done based on the SOSS spectra did not change the assumed QE function at wavelengths greater than 2.1 μm.

The data points were fit with a polynomial function allowing for the weights of the individual points using the mpfit.py and mpfitexpr.py routines (these were taken from http://code.google.com/p/astrolibpy/source/browse/trunk/). The end points were given very small errors to force the fit to pass through these points. The fitting functions were padded with values of 1.0 to cover the full range of the quantum efficiency function, 0.5 to 5.5 μm. A third order polynomial fit is not sufficient to match the points. Going to order 4 allows a fit but the revised quantum efficiency values would be much larger than 1 as shown in the right panel of Figure 10, so this is not an option. The issue as stated in the last section is the high ratio value for the F277W filter. Removing this from the fitting produces a better result, the green curve in the left-hand panel of Figure 10. Multiplying this function by the estimated quantum efficiency produces a new estimate that is found to peak at a value larger than 1.0 around 3 μm as shown in the right-hand panel. An order 5 fit was also tested to see if this would alleviate the issue with quantum efficiency values being estimated as larger than 1, but it gives a higher ratio at wavelengths around 3 μm and this increases the revised quantum efficiency values at these wavelengths. The order 5 fit is the red curve in the left-hand panel of the Figure, and the revision is shown as the red curve in the right-hand panel. It was decided to use the order 4 fit without the F277W value as the best revision for the quantum efficiency values. This still leaves the F277W prediction a bit high, however the recommended LDS 749B model spectrum in the CALSPEC database changed between the initial estimates and the final round of revisions and it turned out that the discrepancy with the measured values was not as large when the values were recalculated using the revised quantum efficiency values and the revised LDS 749B model spectrum.

Although the revised quantum efficiency estimates peak at a value of 1.015 for fit

number 2 in the left-hand panel of Figure 10, this is only slightly higher than the peaks at shorter wavelengths and so it was assumed that this could be fixed in the rescaling once the new OTE throughput values were available. That revision is discussed in Section 11.

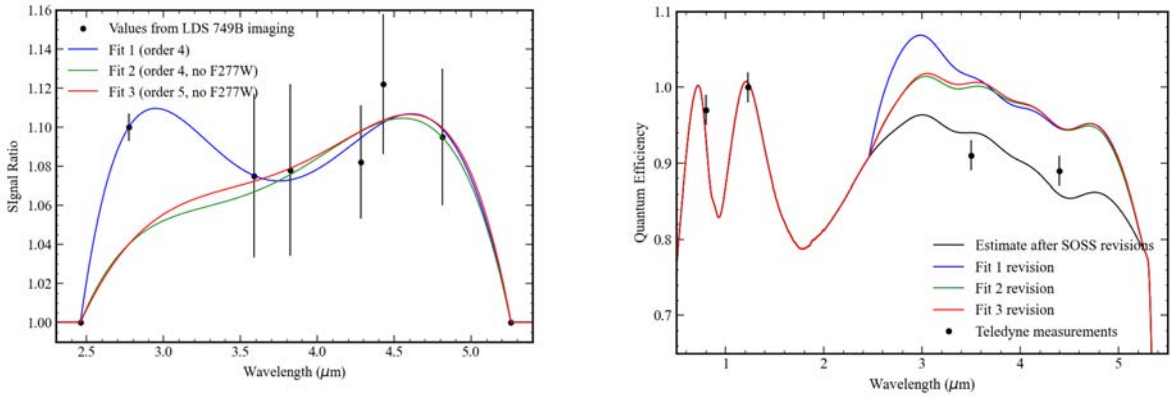

Figure 10: (left panel) The ratio points used for the long wavelength QE fitting, along with some fitting functions. The points are as in Table 2 above, while the pivot wavelength is used for the x axis values, plus fixed end-point values where the ratio is set to 1.0. The fitting functions shown use a weighted least-squares data fit with the end point assigned very small uncertainties. The fitting function is also padded with values of 1.0 to extend it to the range 0.5 to 5.5 μm. (right panel) Comparison of the quantum efficiency revisions from the fits shown in the left panel with the Teledyne measurements.

The estimated quantum efficiency was revised by multiplying it by the "fit 2" ratio values shown in the left panel of Figure 10. Using this revised quantum efficiency estimate the simulated imaging count rates for the LDS 749B model were recalculated. The new values are shown in Table 3. All the revised signal values are within the quoted uncertainties of the measurements from NIS020 except for the case of F277W where the predicted signal is 2.2% low. There were some very small changes to the simulated count rates for the short wavelength filters at approximately the level of a few parts in 10^7 which is some indication of the practical limits on the machine precision in the values of the function.

Table 3: Comparison of the observed and simulated count rates for LDS 749B after the long wavelength quantum efficiency revision.

Filter	Count Rate (ADU/s)	Simulated Count Rate	Ratio Observed/Simulated
F090W	113626±2756	113585.5	1.000±0.024
F115W	84632±1847	83622.32	1.012±0.022
F140M	27074±156	26927.47	1.005±0.006
F150W	50101±393	50127.98	0.999±0.008

Filter	Count Rate (ADU/s)	Simulated Count Rate	Ratio Observed/Simulated
F158M	22617±143	22909.64	0.987±0.006
F200W	28766±307	28868.17	0.996±0.011
F277W	16845±112	16470.88	1.022±0.007
F356W	10584±464	10641.34	0.995±0.047
F380M	1921±80	1923.68	0.999±0.044
F430M	1236±33	1258.49	0.982±0.029
F444W	6697±216	6549.94	1.022±0.036
F480M	1117±36	1118.25	0.999±0.032

There is the option at this point of doing a small scaling of the individual filter response functions to correct the various ratio values to 1.0. In the case of the F277W filter both the SOSS observations and the high current fractional response values make such a 2.2% increase difficult to manage. As most of the ratio values in the Table are small and within the measurement uncertainties no scaling was deemed necessary. Such a revision may become necessary in the future with more observations of standard stars and an improved overall accuracy in the photometric measurements.

Although the revisions to the estimated NIRISS quantum efficiency produce the desired results for the count rate estimates, the new function is now somewhat inconsistent with the Teledyne measurements as shown in the right panel of Figure 10. The various small wiggles on the estimated quantum efficiency curve between 3 and 4.8 μm are probably not real. The overall shape in this wavelength range is unusual compared to the other H2RG detectors in the same manufacturing batch that have good quality quantum efficiency measurements. Despite these possible issues, there does not seem to be an alternative way to adjust the NIRISS component throughputs to match the observations that does not produce unphysical values.

Having changed the estimate of the NIRISS quantum efficiency the SOSS order 1 blaze estimate needs to be revised to compensate and preserve the fit that was made earlier. This is done by simply dividing the GR700XD order 1 response by the fit 2 ratio function in Figure 10. The result of the change is shown in Figure 11 below. Interestingly, the change mostly removes the bump on the GR700XD response that was present at 2.4 to 2.85 μm, although there was no explicit allowance for this in the fitting process.

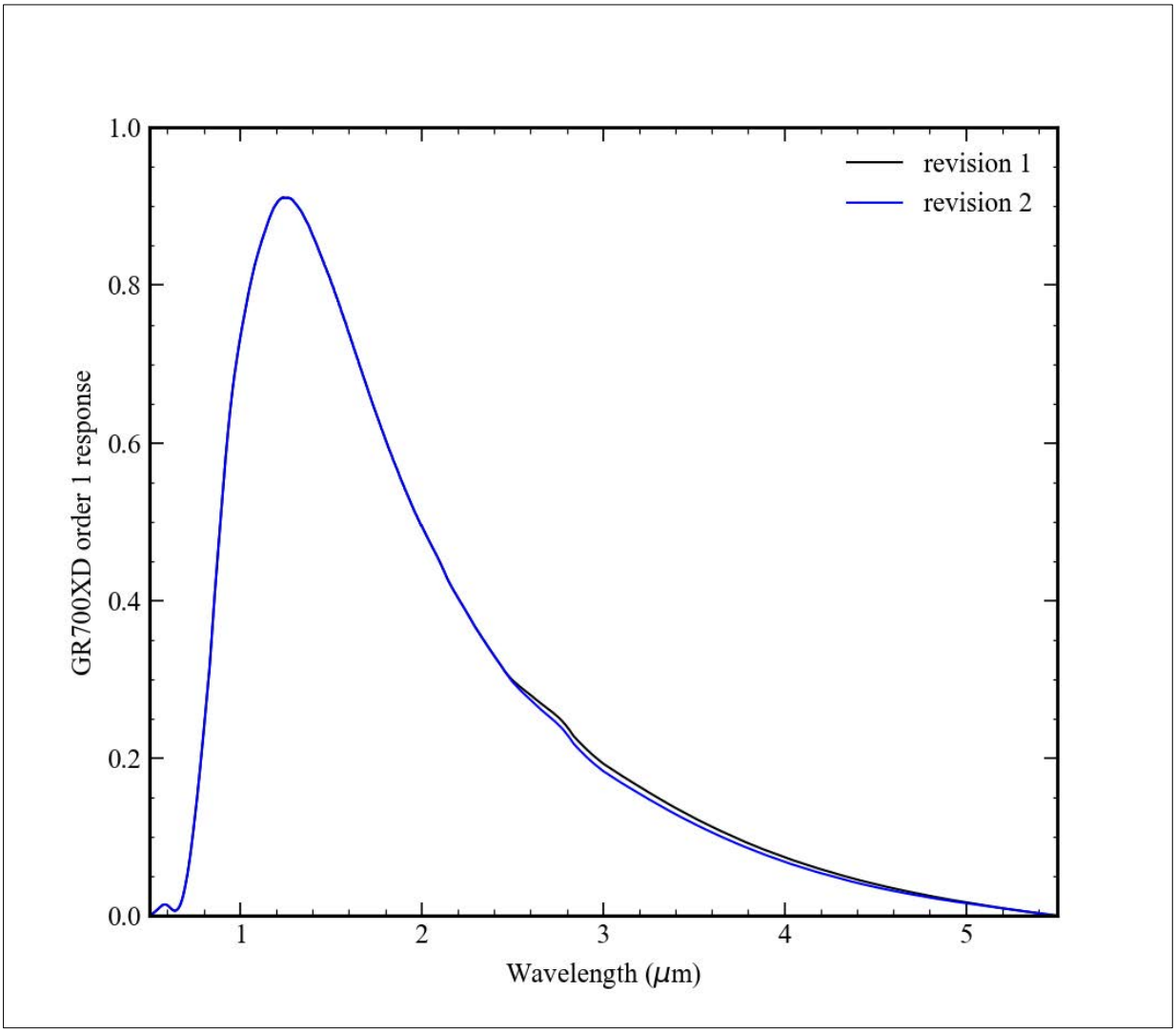

Figure 11: The long wavelength revision to the estimated GR700XD grism response is shown here. The black curve is as in Figure 9 above. The blue curve is the estimated GR700XD order 1 response after the scaling to compensate for the change in the long wavelength quantum efficiency estimate and leave the product of the two response functions same as before.

9 GR150C and GR150R Response Revisions

The final step in the throughput revisions was to derive the changes to the estimate GR150 grism response functions that are needed to match the observations. The pre-flight ETC files had identical inputs for GR150C and GR150R based on measurements of a flight spare grism. The grism was made at the same time as the flight parts and so should give a close approximation to the response of the flight parts. Observations on-sky quickly showed that the GR150C grism has better response than the GR150R grism. An initial determination of the GR150C conversion factors for the F090W filter was checked against the SOSS conversion factors to make sure that the changes in the estimated detector quantum efficiency described in section 5 would not produce bad results for the WFSS mode. Once that check had been done, no further use was made of the WFSS inputs until the SOSS-related throughput revisions were finished and the imaging count rates predictions were compared to the observations to verify the imaging filter response functions.

The WFSS photometric calibration in program used two standard stars in the observations: WD 1657+343 and GSPC P330-E. For the analysis here the response function from the observations of WD 1657+343 were used. Due to time constraints no comparison was made with the GSPC P330-E observations in the program, which were taken in calibration subarrays that are not used for WFSS science observations.

For WFSS each filter samples only a part of the grism response. The method used was to change the conversion factors in Jy/(ADU/s) to total photon conversion efficiency values and then compare these with the revised predictions from the response files for each grism, filter, and order where the values had been measured. The same general process was used for the WFSS grisms as for the GR700XD case: in each order, the ratio of the observed to the predicted total photon conversion efficiency values was taken to be a correction factor for the grism blaze function. In first order the ratio values were assembled for each of the 6 blocking filters in each grism, and then a fit was made to the combined set of points. In second order only the F090W filter had the response measured, so that was dealt with by itself.

The S/N of the photometric calibration was not as high in the WFSS case as in the SOSS case, primarily because in the SOSS case a short time series observation was done and this provided better S/N than what was obtained in the "normal" measurement of the photometric response in the program. In WFSS mode the spectra were extracted using a fixed cross-dispersion box size of 15 pixels, and aperture corrections were applied using WebbPSF models. The derivation of the conversion values was done by Swara Ravindranth and the values were then passed to Kevin Volk for packing into the pipeline reference file.

For each WFSS grism the order 1 ratio values for all the filters were fit together with a polynomial function of wavelength to produce a smooth correction function. For order 2 with only the single filter values a linear fit was made to the ratio values. The expected peak of the GR150 order 2 response is at somewhat shorter wavelengths than the response of the F090W filter. This makes extrapolation of the order 2 changes to longer and shorter wavelengths very uncertain. Figure 12 through Figure 15 show the ratio values and the fit functions for the two grisms and the two orders.

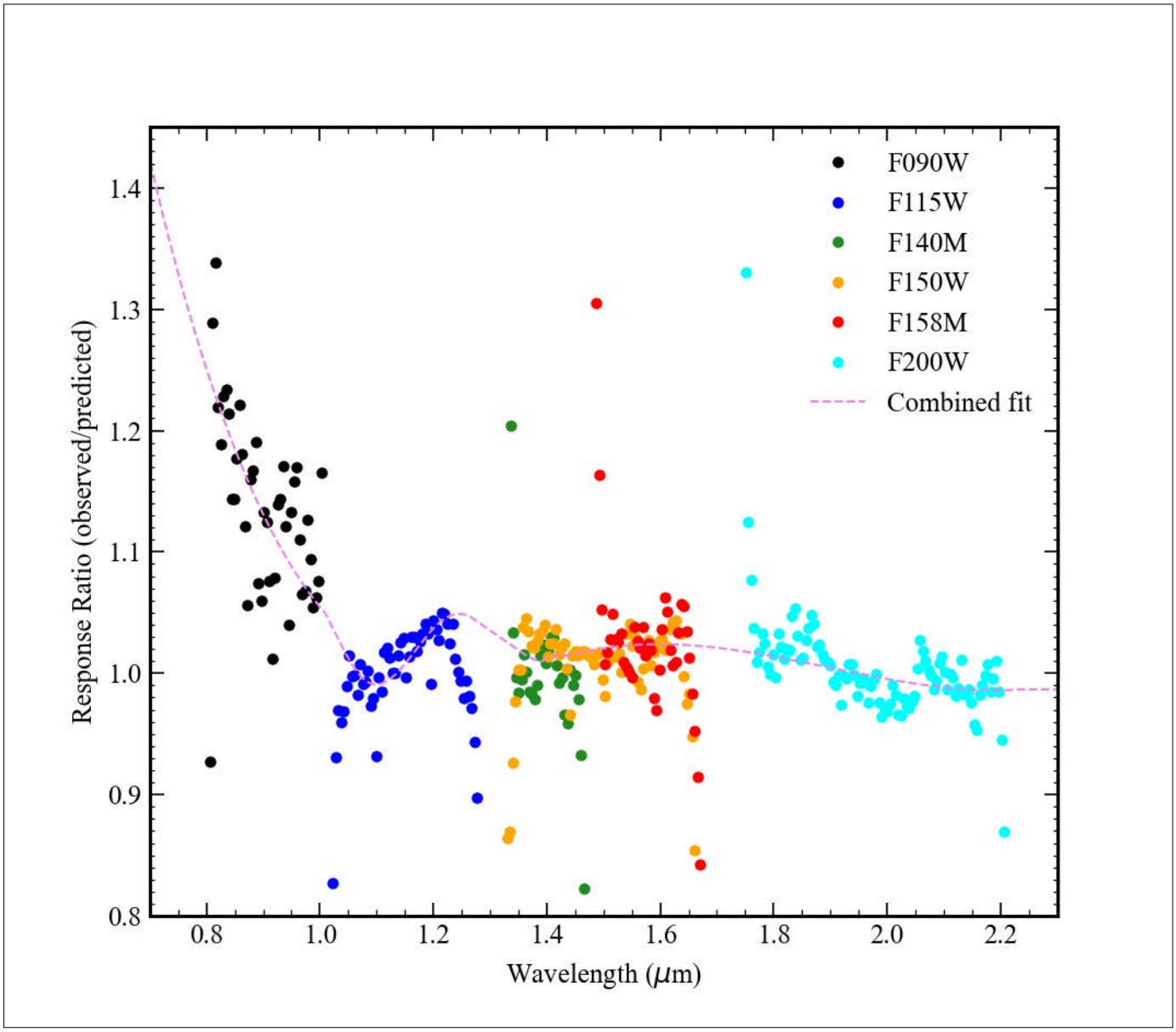

Figure 12: The response ratio values for the GR150C grism in first order from the six blocking filters, plus a fitting function derived from these values. One sees significant edge effects in most of the filters so these points were not included in the fitting.

For both grisms the longer wavelength ratio values in the fit were adjusted to produce a constant ratio value at wavelengths above about 2.2 μm. The fits were also linearly extrapolated from the short wavelength end of the F090W filter to 0.5 μm. In the case of the GR150C grism one could question whether the local feature peaking at 1.2 μm is real, although the F115W data does suggest such a rise. It was difficult to produce a fit to the data points that gave a good result in the F115W filter region using either a low order polynomial or a low order spline fit. For the fit to the GR150R values the polynomial fit has a shallow minimum at 1.2 μm which again may not be real…it was difficult to accommodate the rise in the F090W points, the dip in the shorter wavelength part of the F115W filter values, and the relatively flat response in the other filters and the longer wavelength part of the F115W filter with a low

order polynomial or spline fit. It is hoped that with additional photometric data in the future this situation can be improved. The amount of scatter in the F115W points in particular does not match the estimated S/N of the observation. If seems likely that the wavelength solution needs some further improvement to reduce the scatter in these points.

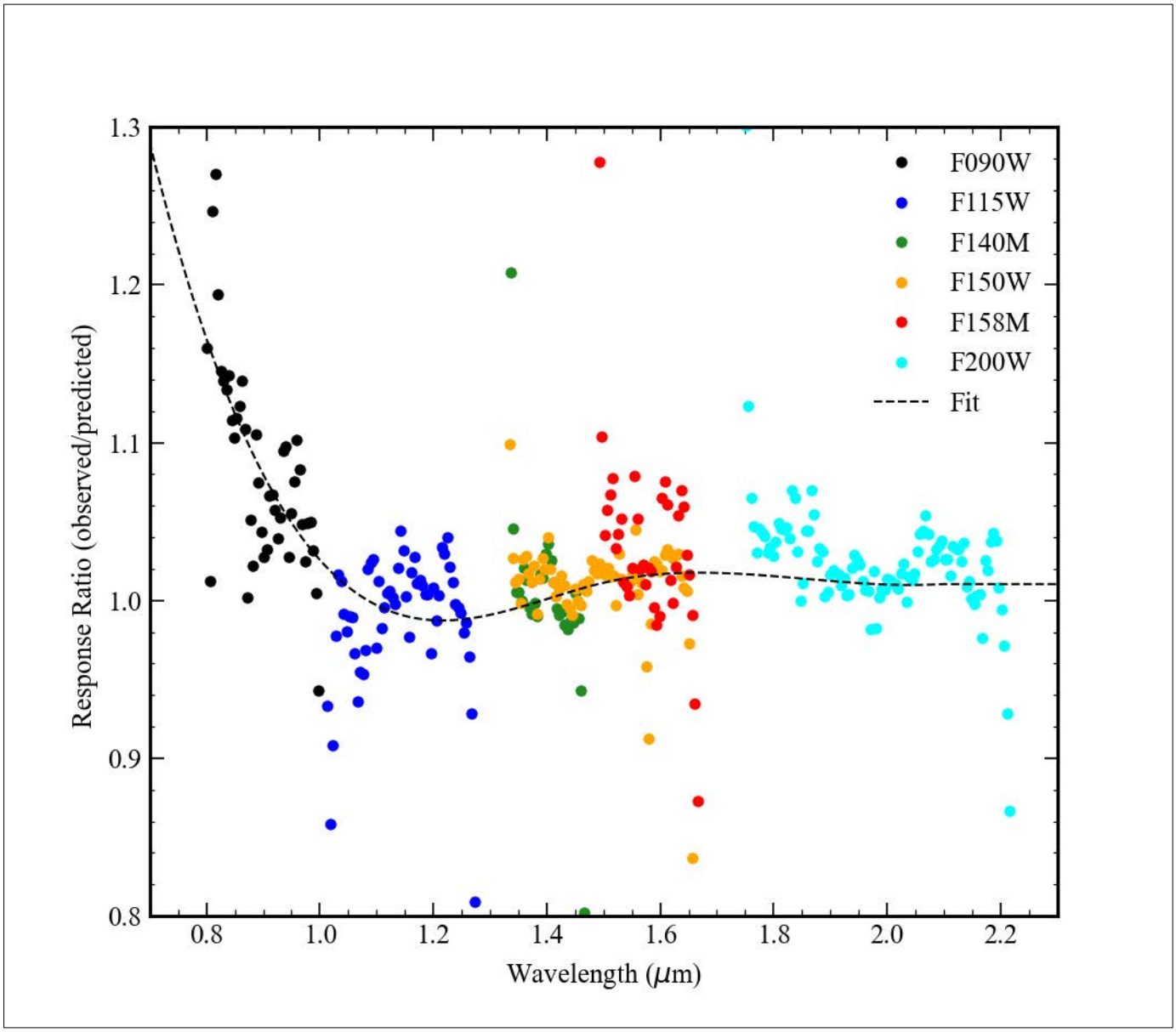

Figure 13: The response ratio values for the GR150R grism in first order from the six blocking filters, plus a fitting function derived from these values. One sees significant edge effects in most of the filters so these points were not included in the fitting.

The situation in second order is uncertain, mostly because of the small wavelength range involved since only the F090W filter second order spectrum was calibrated. The second order spectrum in most of the other filters is very weak because of the first order blaze peak between the F115W and F140M filter response ranges. With only results for F090W the linear fit that was determined was extrapolated to 1.0 at longer wavelengths and thereafter fixed at

1.0. At shorter wavelengths the linear fit was simply extrapolated to the minimum wavelength of 0.5 μm. The peak of the second order response is expected to occur not too much shorter in wavelengths than the cut-off of the F090W filter, but we have no data from on-orbit that is able to verify this.

Figure 16 and Figure 17 show the revised order 1 and order 2 blaze functions after the ratio scaling has been applied for the two grisms, along with the pre-flight curves for comparison. The peak of the GR150R order 1 blaze function is not changed significantly but the wavelength is shifted to slightly shorter wavelengths. The order 1 blaze peak for GR150C comes out higher by roughly a factor of 1.035 than was expected prior to flight and is shifted further to short wavelengths. The peaks of the order blaze functions are 1.269 μm for GR150C and 1.381 μm for GR150R. For order 2 both grisms have revised responses that are somewhat lower than originally estimated, although this is subject to significant uncertainties.

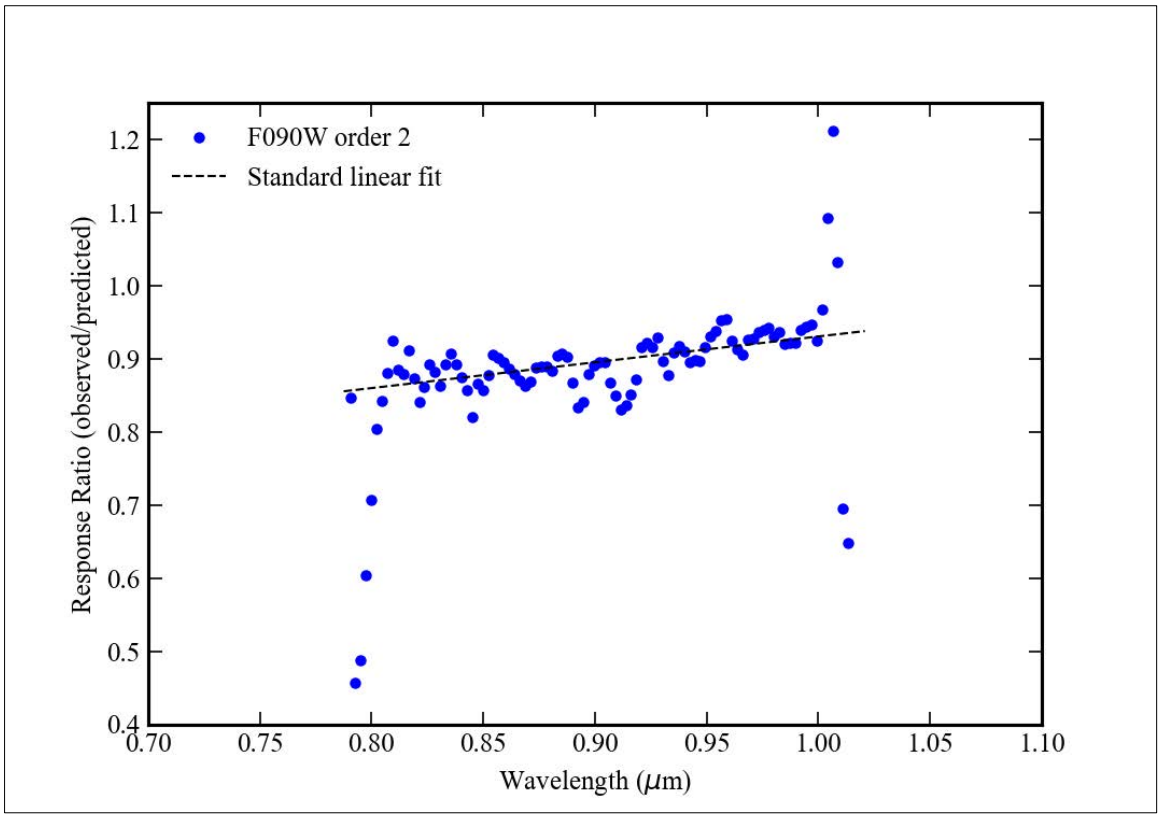

Figure 14: The response ratio values for the GR150C grism in second order from the F090W filter, plus a linear fit derived from these values. One sees significant edge effects in the data values so these points were not included in the fitting.

In some cases, the commissioning observations in WFSS mode show order 2 for filters other than F090W or other orders, order 3 and higher orders and order –1 and lower orders. In these instances, the first order spectra are generally saturated so absolute calibration of these other orders cannot be directly obtained. The order 0 "spectra" are commonly seen, but in this case since there is no wavelength information and the "spectrum" usually looks identical to a point source in the direct images to the limits of our ability to measure the profile the best description is to give a scaling value from the direct image signal to the dispersed order 0 signal. These types of measurements are of concern in describing the contamination of the

additional orders in the science orders, but that analysis has not yet been done. When this contamination analysis is done, it may lead to some revisions in the order 2 response functions for the grisms.

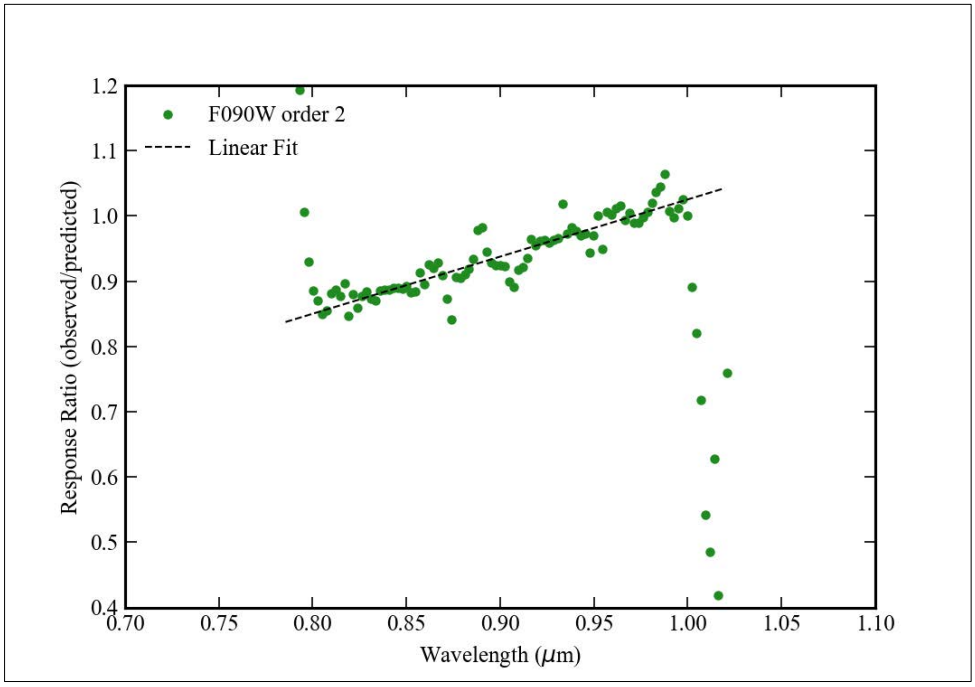

Figure 15: The response ratio values for the GR150R grism in second order from the F090W filter, plus a linear fit derived from these values. One sees significant edge effects in the data values so those points have been excluded from the fit.

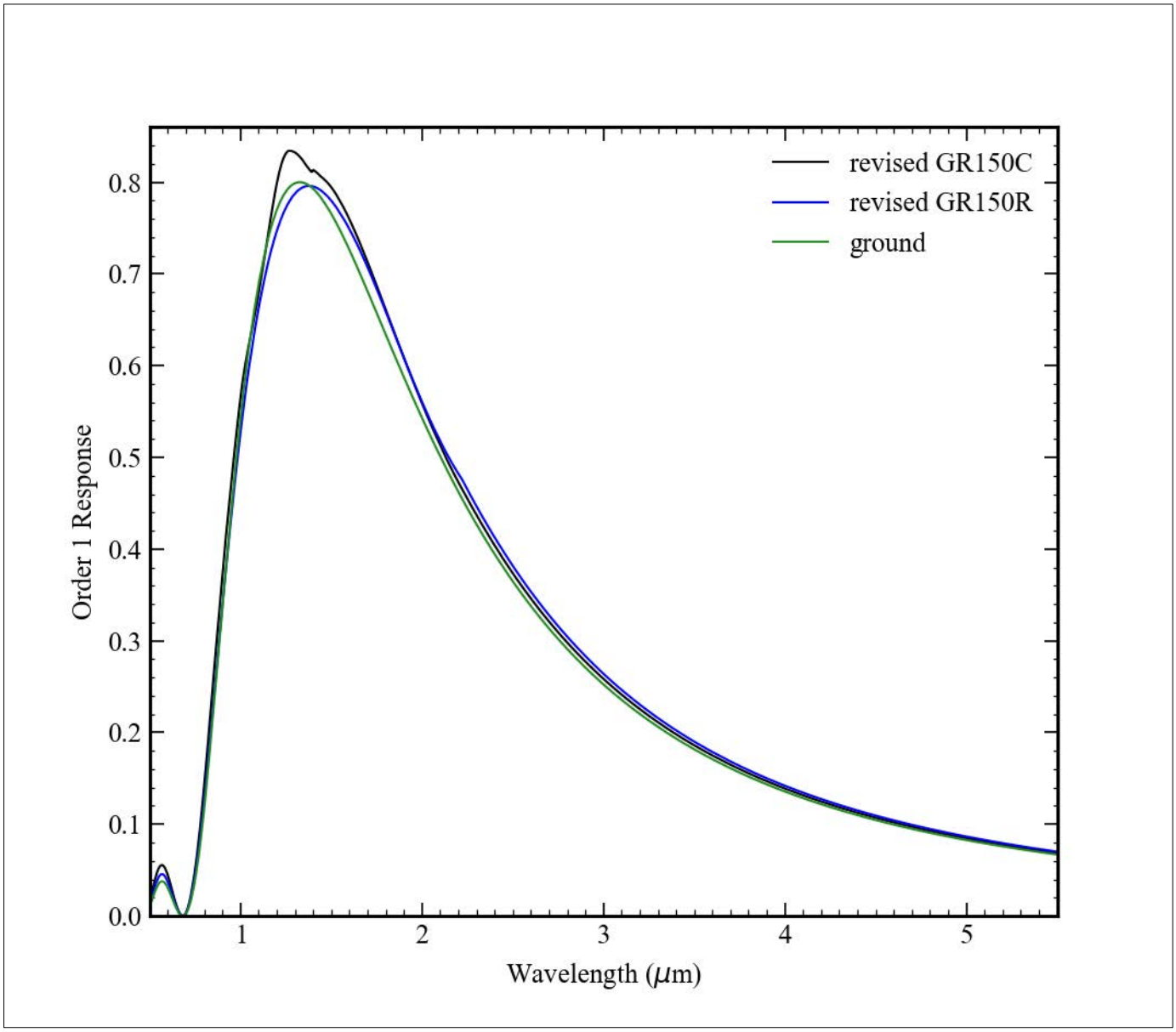

Figure 16: The revised order 1 blaze functions for GR150C and GR150R from the ratio value fits shown in Figure 12 and Figure 13 are plotted along with the pre-flight blaze function.

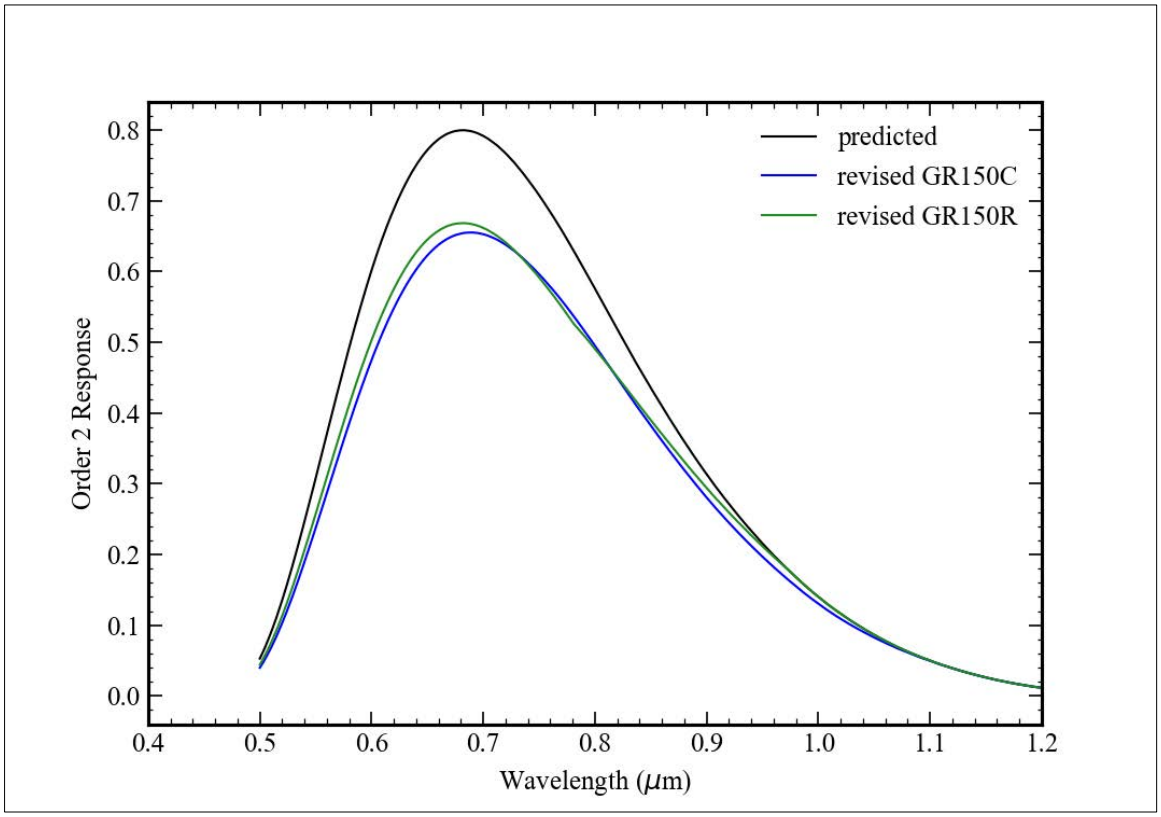

Figure 17: The revised order 2 blaze functions for GR150C and GR150R from the ratio value linear fits shown in Figure 14 and Figure 15 are plotted along with the pre-flight blaze function. The extrapolations from 0.8 μm to 0.5 μm are quite uncertain for both grisms. In both cases the scaling values were extrapolated linearly to a maximum of 1.0 at longer wavelengths. Limiting the scaling to a maximum of 1.0 is also uncertain due to the lack of measurements in the longer wavelengths.

10 Changes to Photometric Quantities

The changes in the estimated NIRISS throughput have effects on the imaging photometric calibration quantities related to magnitude conversion. The magnitude system used for NIRISS is based upon use of the Sirius template spectrum from CALSPEC to define the zero-magnitude flux density and count rate, assuming that Sirius has a magnitude of –1.395 in the NIRISS filters. The zero magnitude count rates are estimated from simulations because we cannot observe Sirius directly with NIRISS in any of the observing modes. The rationale for the magnitude assigned to Sirius in the JWST filters is discussed in Rieke et al. (2022). Table 4 given below shows values of the zero-magnitude flux density values calculated using the pre-flight and on-orbit throughput functions and the 2020 Sirius model, along with the pivot wavelength values. These are all calculated as per equations (1) and (3) above.

Table 4: Comparison of the calculated zero magnitude flux density values and pivot wavelength values for the pre-flight and revised total photon conversion efficiency estimates.

Filter	Pivot Wavelength (pre-flight estimate, μm)	Pivot Wavelength (revised estimate, μm)	Zero Magnitude Flux Density (pre-flight estimate, Jy)	Zero Magnitude Flux Density (on-orbit estimate, Jy)	Ratio
F090W	0.90246	0.90011	2316.42	2318.88	1.0011
F115W	1.14954	1.15180	1800.89	1795.54	0.9970
F140M	1.40404	1.40386	1316.42	1316.64	1.0002
F150W	1.49346	1.49151	1202.65	1205.08	1.0020
F158M	1.58201	1.58062	1090.05	1091.72	1.0015
F200W	1.99296	1.98676	762.53	766.46	1.0052
F277W	2.76428	2.77865	435.99	432.68	0.9924
F356W	3.59300	3.59107	270.93	271.32	1.0014
F380M	3.82523	3.82507	236.88	237.24	1.0015
F430M	4.28383	4.28399	191.57	191.58	1.0000
F444W	4.42770	4.42802	183.04	182.99	0.9997
F480M	4.81524	4.81440	154.46	154.58	1.0008

The largest changes are seen in the F200W and F277W filters, both at the 0.5% to 0.7% level. The changes are all a result of the combined estimated internal optics and detector efficiency values since no changes were made to the pre-flight filter response estimates. Presumably there was some small change in the F277W ratio value from the removal of the water ice absorption factor, but the ratio value for F277W is smaller than 1.0 so the change in the long wavelength quantum efficiency estimate is offsetting any change from the water ice feature. The F277W filter does have a small response in a narrow wavelength range around 0.85 μm (verified in the SOSS observations with this filter) that may also be affecting the ratio since there was a larger change to the quantum efficiency estimate at these wavelengths than at the longer wavelengths. Note that the zero magnitude flux density values are not affected by a global scaling of the throughput values so it is the changes in relative response over the filter that change the zero magnitude flux density estimates.

Using the new response functions and the 2020 Sirius model from CALSPEC the zero magnitude count rate values can be calculated. The resulting values are given in Table 5 along with the magnitude for a count rate of 1 ADU/s. The offsets from AB magnitude values to the Sirius-based magnitude values are also listed. In the JWST pipeline output flux density values in Jansky are calculated for the sources when a source catalogue is made, and these are converted to AB magnitudes. The AB magnitudes are offset to a "Vega magnitude" value as well. The values in the last column in Table 5 are used to make a reference file for the JWST pipeline.

Table 5: The zero magnitude count rate values estimated for the NIRISS filters based upon the response functions and the 2020 Sirius model from CALSPEC. These are for the normal magnitudes with a nominal A0V colour of 0.0 between filters.

Filter	Zero Magnitude Count Rate (ADU/s)	Magnitude for 1 ADU/s	AB to A0V Magnitude Offset
F090W	9.3736e+10	27.4298	–0.486868
F115W	7.7172e+10	27.2187	–0.764579
F140M	2.5322e+10	26.0087	–1.101397
F150W	4.7322e+10	26.6876	–1.197529
F158M	2.1696e+10	25.8381	–1.304784
F200W	2.8592e+10	26.1406	–1.688843
F277W	1.6718e+10	25.5580	–2.309654
F356W	1.1033e+09	25.1068	–2.816350
F380M	1.9864e+09	23.2452	–2.962097
F430M	1.3140e+09	22.7965	–3.194173
F444W	6.8348e+09	24.5868	–3.243989
F480M	1.1706e+09	22.6710	–3.427191

The term “Vega magnitude” is used by the Hubble Space Telescope instruments, since Vega can be used for the direct calibration of HST. For JWST this term is somewhat misleading since Sirius is used as the fiducial A0V stellar template for the magnitude definitions. Note that the AB to A0V magnitude offset value as listed has the opposite sign to what is used in the pipeline reference file for the source catalogue step. The offset values listed here are to be added to the AB magnitude to produce the A0V magnitude.

11 OTE Throughput Revisions

A revision to the estimated OTE throughput values was provided by Marshall Perrin on 23 August 2022. The revision produced changes up to 3% at maximum for the OTE throughput function over the NIRISS wavelength range, but the change was a reduction in estimated response at some wavelengths and an increase in the estimated response at other wavelengths.

For the NIRISS ETC files it is necessary to make revisions to the values so that the product of the OTE throughput function, the internal optics throughput function, and the detector response function is unchanged. It is also necessary to reduce the peak quantum efficiency below 1.0 since the peak at 1.01 derived from the SOSS photometry values is unphysical.

Figure 18 shows the ratio function over the NIRISS wavelength range. The values in the OTE throughput function were determined at a discrete set of wavelengths and then a smoothed function was fit to these values, so the ratio function shows various linear segments between what I assume to be the anchor points.

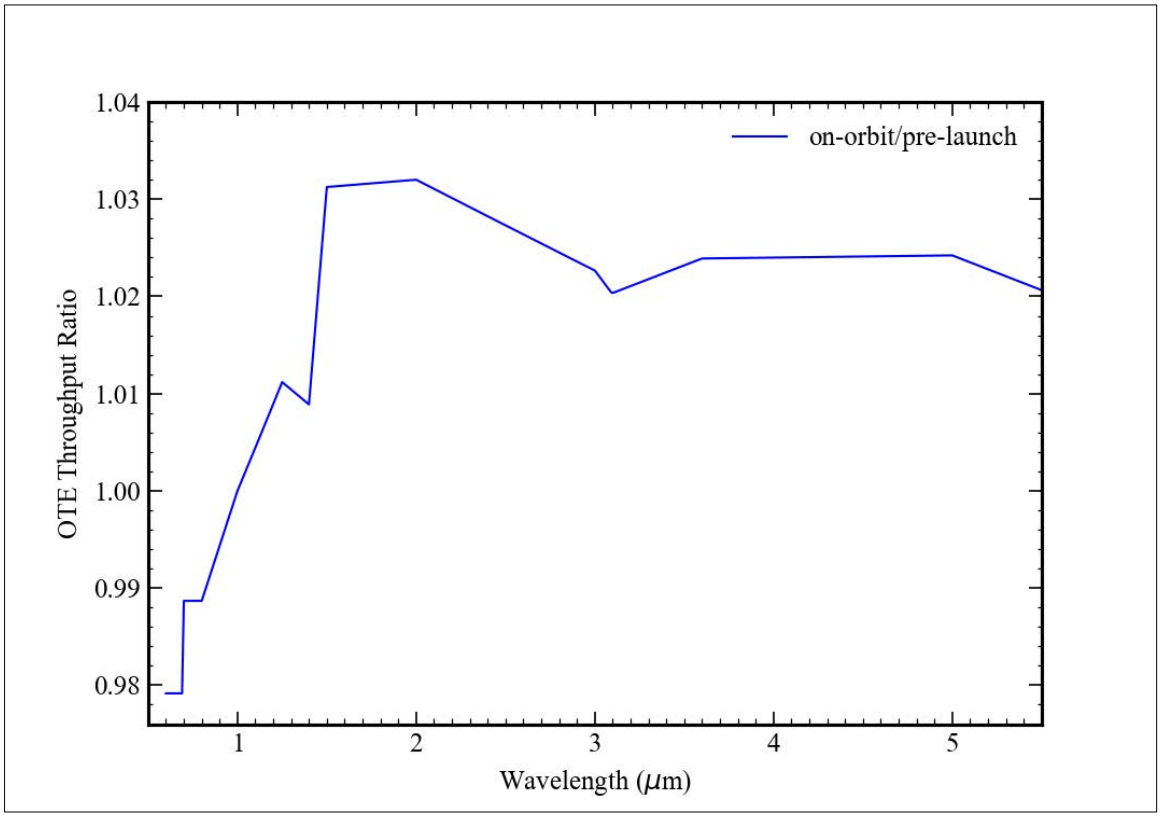

Figure 18: The ratio of the revised OTE throughput estimate provided on 23 August 2022 to the previous estimates currently used in the ETC and for the NIRISS count rate simulations. The plot is limited to the NIRISS wavelength range. The values are less than 1.0 for wavelengths below about 1 μm.

One cannot simply apply the inverse of this ratio function as a correction to the NIRISS quantum efficiency estimates because the values are less than 1.0 at short wavelengths where one of the quantum efficiency peaks is located (see Figure 5 above). The hope had been that the OTE revisions would have ratio values above 1.0 at the short wavelengths so that the correction would bring the quantum efficiency values all below 1.0, but if the inverse of the OTE ratio is used to correct the quantum efficiency values the new values peak at 1.0172.

The requirement is that the product of the OTE throughput, the internal optics throughput, and the detector quantum efficiency be kept fixed at each wavelength. How the values are split up is not important for the ETC calculations. The method that was applied was to first calculate the product of the pre-flight OTE throughput times the revised quantum efficiency times the internal optics throughput, which needs to be kept fixed. The quantum efficiency function was then reduced by 2% at all wavelengths to have a peak value that is less than 1. The throughput product was then divided by the new quantum efficiency function and by the new OTE throughput function to produce a revised internal optics function. The result of these revisions is shown in Figure 19.

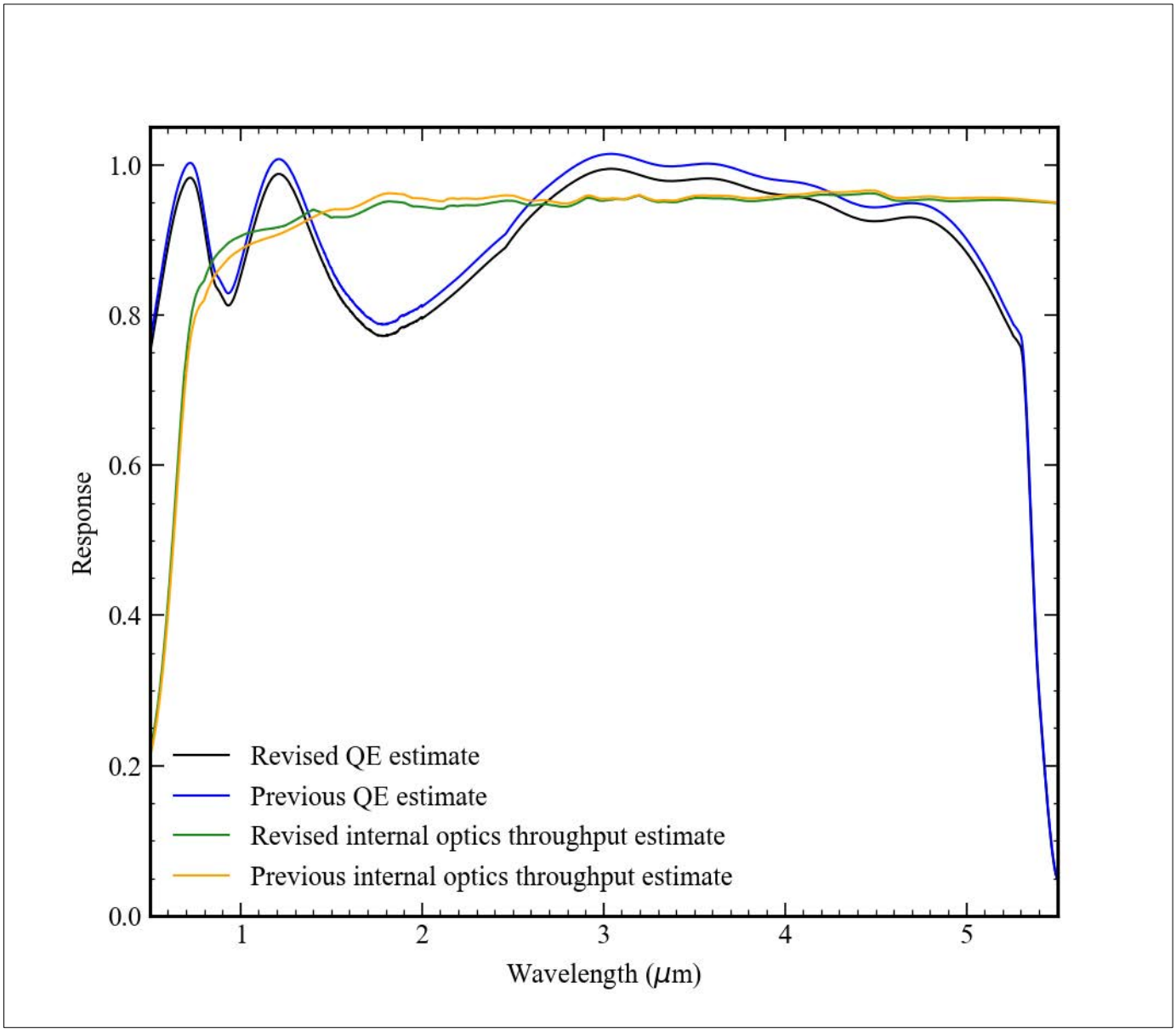

Figure 19: The effect of revisions on the NIRISS quantum efficiency estimate and the internal optical throughput estimate to allow for the change in the estimated OTE throughput values. The quantum efficiency function was reduced 2% independent of wavelength and the internal optics function was adjusted to offset that change along with the changes to the OTE throughput estimate.

The result of the changes to the internal optics throughput function is an increase at the short wavelengths, particularly from 0.7 to 1.3 μm, a small decrease between about 1.5 and 2.7 μm, and not much change at the longer wavelengths. The internal optics response at long wavelengths is a bit higher than one might expect, of order 0.96 overall with 7 reflecting surfaces such that the individual surface reflectivity must be close to 0.994. This might be an indication that the detector quantum efficiency estimate is too low at the longer wavelengths and should be increased by a few percent where this is possible, say starting at a wavelength of 3.5 μm, and the internal optics throughput estimates decreased to match. Since we have no way to make any independent measurements of the two functions at these wavelengths, and

since in particular there is no spectroscopic data to test whether the shape of the combined response curve is correct, this question is judged to be moot at this stage.

12 Conclusions

Using the photometric measurements for the NIRISS science modes in commissioning a set of revisions to the estimates of the NIRISS internal throughput have been carried out. For the imaging case only an overall scaling factor has been applied to the pre-flight filter response measurements. For the grism modes a series of revisions were made to the estimated response of the NIRISS internal optics, the NIRISS detector response, and the grism response functions in each observed order. The combined set of new response estimates will be delivered to the JWST exposure time calculator for estimation of the NIRISS count rates and S/N in observations. The values derived from the NIRISS observations were corrected for the revisions to the estimated OTE throughput provided by the telescopes group after the initial set of NIRISS revisions had all been done.

There remain uncertainties in the GR150C and GR150R response corrections because the scatter in the observed values for these grisms was at the few percent level, higher than the target S/N of the photometric observations. Additional photometric observations in the WFSS mode in cycle 1 and beyond will be needed to improve the quality of the corrections to the GR150 blaze functions.

13 References

Bohlin, R. C., Gordon, K. D., and Tremblay, P.-E., 2014, PASP, 126, 711.

Darveau-Bernier, A., Albert, L., Van Talens, G., et al., 2022, PASP, 134**,** 094502.

Goudfrooij, P., et al., 2022, technical report in preparation.

Perrin, M. D., Sivaramakrishnan, A., Lojoie, C.-P., Elliott, E, Pueyo, L., Ravindranath, S., and Albert, L., 2014, Proc. SPIE. 9143.

Rieke, G. H., Su, K., Sloan, G. C., and Schlawin, E., 2022, AJ, 163, 45.